ELECTROMAGNETIC CHARACTERIZATION OF INHOMOGENEOUS MEDIA

THESIS

Marcus A. Sitterly, Captain, USAF

AFIT/GE/ENG/12-37

DEPARTMENT OF THE AIR FORCE
AIR UNIVERSITY

AIR FORCE INSTITUTE OF TECHNOLOGY

Wright-Patterson Air Force Base, Ohio

APPROVED FOR PUBLIC RELEASE; DISTRIBUTION UNLIMITED

The views expressed in this thesis are those of the author and do not reflect the official policy or position of the United States Air Force, Department of Defense, or the United States Government. This material is declared a work of the U.S. Government and is not subject to copyright protection in the United States.

AFIT/GE/ENG/12-37

ELECTROMAGNETIC CHARACTERIZATION OF INHOMOGENEOUS MEDIA

THESIS

Presented to the Faculty

Department of Electrical and Computer Engineering

Graduate School of Engineering and Management

Air Force Institute of Technology

Air University

Air Education and Training Command

In Partial Fulfillment of the Requirements for the

Degree of Master of Science in Electrical Engineering

Marcus A. Sitterly, B.S.E.E
Captain, USAF

March 2012

APPROVED FOR PUBLIC RELEASE; DISTRIBUTION UNLIMITED

AFIT/GE/ENG/12-37

ELECTROMAGNETIC CHARACTERIZATION OF INHOMOGENEOUS MEDIA

Marcus A. Sitterly, B.S.E.E

Captain, USAF

Approved:

//Signed//	09 Mar 2012
Dr. Michael J. Havrilla (Chairman)	Date
//Signed//	09 Mar 2012
John Dea, Lt Col, USAF (Member)	Date
//Signed//	12 Mar 2012
Maj. Milo W. Hyde, Ph.D. (Member)	Date

AFIT/GE/ENG/12-37

Abstract

Material permittivity and permeability parameters dictate how a given material will react when subjected to electromagnetic fields. Simple media have been studied in great depth, and describe how linear, homogenous, and isotropic materials behave. Complex materials, those of which deviate from simple media in linearity, homogeneity, and isotropy, can react to electromagnetic fields in ways that differ greatly from simple media.

Due to this fact, research is done to better understand these types of materials. The research in this study focuses on one aspect of complex media: inhomogeneity. The purpose is to develop an algorithm that finds the inhomogeneous permittivity profile of a material along its z-axis using rectangular waveguide measurements. This is accomplished by obtaining scattering parameters in the laboratory and using a Levenberg-Marquardt root search algorithm to extract the material's inhomogeneous permittivity profile.

The inhomogeneous problem is approached in two unique ways. The first method employs a discrete approach in which the material is assumed to be comprised of piece-wise constant permittivity sections. This allows the use of simpler homogeneous wave equations. The second method is a continuous approach which uses inhomogeneous wave equations to find a linear permittivity profile.

Acknowledgments

No accomplishment is made without the help, dedication, and hard work of others. I am indebted to the work and support of my committee, professors, experts, friends, and family. The sum efforts of countless people have made this research possible.

First I would like to give a special thanks to my advisor, Dr. Havrilla. His articulation of the physical behavior of electromagnetic fields and waves has made these once difficult concepts intuitive. Without his expertise this research would have been a much larger mountain to climb.

Also, I would like to take the opportunity to thank everyone who made it possible for me to attend the Air Force Institute of Technology. This has been an outstanding experience that allowed me to focus on research without the competing demands of additional duties, and gave me the opportunity to build depth in my understanding of engineering that I could not have otherwise obtained.

I would like to especially extend gratitude to my wife. Her unique perspective and incredibly supportive nature is inspirational. Without her love and sacrifice, this would have been a much more demanding and difficult process.

And finally I would like to thank God, the source of all good. His qualities of love and intelligence have been felt throughout this process.

Marcus A. Sitterly

Table of Contents

Page

Abstract iv

Acknowledegments iv

Table of Contents vi

List of Figures viii

I. Introduction 1

1.1 Assumptions & Scope 2

1.2 Materials & Equipment 3

1.3 Literary Foundation 4

1.4 Thesis Overview 5

II. Discrete Characterization 6

2.1 Discrete Theory Development 8

2.2 Constitutive Parameter Extraction 13

2.3 Summary 19

III. Continuous Characterization 20

3.1 Forward Measurement Field Descriptions 21

3.2 Forward Measurement Transmission and Reflection Coefficients. 30

3.3 Reverse Measurement Field Descriptions 34

3.4 Reverse Measurement Transmission and Reflection Coefficients. 35

3.5 Numerical Computations of Slope and Intercept 34

3.6 Summary 34

IV. Analysis & Results 38
4.1 Experimental Set up 40
4.2 Calibration and Measurements 44
4.3 Error Analysis.....48
4.4 Algorithm Results.....48
4.5 Discrete and Continuous Algorithm Comparison 60
4.6 Summary.....60
V. Conclusion 61
5.1 Future Research 61
Appendix A: Constitutive parameter extraction main code example 63
Appendix B: Code for nlinfit function.....65
Bibliography 67

List of Figures

Figure Page

1.1 Characterization of inhomogeneous material with unknown profile.....3

2.1 Piece-wise constant permittivity profile characterization.....7

2.2 Reflection and transmission of waves through a single interface.....9

2.3 Reflection and transmission of waves in a multi-layered system.....11

2.4 Sliding short measurements.....15

3.1 Linear inhomogeneous profile with forward and reverse incident waves.....21

3.2 TE_{10} modes in WR-90 waveguide.....25

4.1 Network analyzer.....42

4.2 Short, sample holder, and materials.....42

4.3 Shim offsets.....43

4.4 Single port measurements for the discrete approach.....43

4.5 Two port measurement for the continuous approach.....44

4.6 Left justified and right justified sample measurements.....46

4.7 Real and imaginary results for Plexiglass.....50

4.8 Real and imaginary results for laminate.....51

4.9 Real and imaginary results for mica.....51

4.10 Real and imaginary relative slopes for Plexiglas.....53

4.11 Real and imaginary results for blue paper.....53

4.12 Real and imaginary results for yellow plastic.....54

4.13 Plastic and paper inhomogeneous material construction.....54

4.14 Continuous algorithm relative intercept results 55

4.15 Continuous algorithm relative slope results.....56

4.16 Continuous algorithm profile results 57

4.17 Discrete algorithm profile results.....57

4.18 Inhomogeneous material characterized with homogeneous algorithm.....58

4.19 Inhomogeneous material profiled with homogeneous algorithm 58

ELECTROMAGNETIC CHARACTERIZATION OF INHOMOGENEOUS MEDIA

I. Introduction

A material's permittivity and permeability characteristics affect scattering of applied electromagnetic waves. These constitutive parameters influence the material's behavior, whether it will act as a dielectric, magnetized material, or conductor. The following paragraphs provide the reader with a brief description of background concepts pertaining to this discussion. For a more detailed study the reader is referred to [2].

Simple materials are linear, homogeneous, and isotropic. These descriptions illustrate how the permittivity and permeability parameters behave within the material. A linear media is one in which the constitutive parameters are not functions of the fields, meaning regardless of the applied field strength, the parameters will remain unchanged. Homogeneity describes constitutive parameters that are constant with respect to their position within the material. Finally, an isotropic media is one in which the parameters are not dependent on field orientation.

Complex materials on the other hand, can be nonlinear, inhomogeneous, non-isotropic, or a combination of these. Nonlinear materials have functional dependence on field strength, inhomogeneous profiles have varying constitutive parameters with respect to position, and non-isotropic characteristics define permittivities and permeabilities that are functions of field direction.

A constant dielectric profile is not always possible due to manufacturing inconsistencies in the material fabrication process. For this reason, a media that was intended to be homogeneous may instead be inhomogeneous. Averaging occurs when using homogeneous methods to characterize these inhomogeneous materials. This leads to an incorrect model when studying electromagnetic scattering and absorption. Due to this fact, research is necessary to enable the correct characterization of inhomogeneous materials. This study focuses on developing a characterization algorithm to extract the profile of a material that is inhomogeneous in one dimension.

1.1 Assumptions & Scope

Although the procedures used in this analysis could easily be extended to include permeability and permittivity, this research focuses only on determining the permittivity profile of a non-magnetic inhomogeneous material. The study also assumes that the material is only inhomogeneous, and does not contain any other complex behavior.

The problem is approached using discrete and continuous methods shown in Figure 1.1. In the continuous case the material with a given thickness, d is assumed to have a linear permittivity profile with a slope m_ε, and intercept ε_{r1}. In the discrete case the material is described using a piecewise constant model where each section has a particular permittivity ε_n, and a total of N permittivity sections are calculated simultaneously.

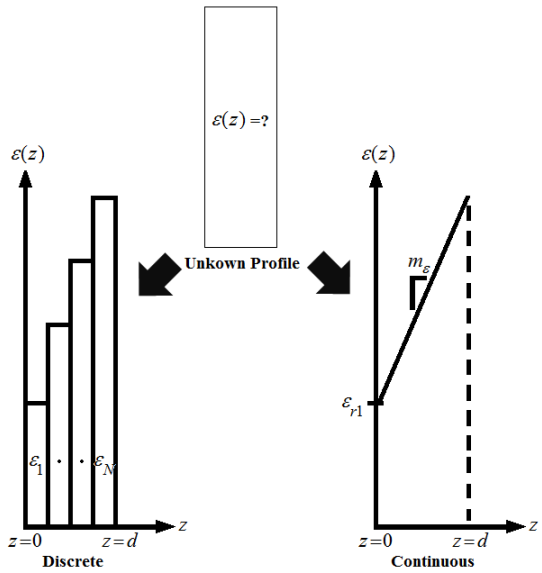

Figure 1.1: Characterization of inhomogeneous material with unknown profile

1.2 Materials & Equipment

A number of resources were necessary to accomplish this research. The Agilent Technologies network analyzer was used to measure scattering parameters used in the profile extraction codes. Various test materials were also needed including Plexiglas, mica, and laminate for algorithm testing. A sample holder and a WR-90 waveguide were used to obtain data in the X-band frequency range of 8.2-12.4 GHz. The discrete method research required additional parts including a short and shim plates which were machined at the AFIT fabrication shop. Finally, this study required the use of facilities such as the microwave laboratory for taking necessary measurements.

1.3 Literary Foundation

There is considerable work on constitutive parameter extraction for homogeneous materials. These methods typically rely on the reflection and transmission coefficients and offer a basis for this work. Additionally, methods have been developed to determine profiles of stratified media in which a single layer has unknown constitutive parameters.

A TEM fixture was used in [9] to find the relative permittivity and permeability of a material. An analytical formulation of the scattering parameters was developed and used for this method. These scattering parameters are functionally dependent on frequency and time delay of the transmitted and reflected waves through a medium. This development provided a means for constitutive parameter extraction.

With the advent of more powerful computers, new methods for solving these parameters were discovered which utilized root search algorithms [12]. This involves the use of scattering parameters as done before, except the material's constitutive parameters are analytically difficult to solve. The root search alleviates this issue by using a theoretical development and experimental data to extract the desired parameters.

The field was further developed when a direct method for parameter extraction was discovered [8]. This method was used to find the constitutive parameters of media between two known materials. This also approach was also based on a root search, and used an $\boldsymbol{A}$ matrix development which is closely related to the scattering parameters measured experimentally. This multi-layered approach provides a significant basis for this work, since the discrete approach in this document uses a stratified like model for inhomogeneous material characterization.

1.4 Thesis Overview

A discrete theoretical development is formulated in Chapter 2. This theoretical formulation is developed for use in a discrete root search algorithm. This algorithm numerically extracts the discrete permittivity profile of an inhomogeneous material using laboratory measurements.

Chapter 3 describes the theoretical background for the continuous approach. Much like the discrete theory, this continuous theoretical framework was implemented in code, and a root search algorithm was used to extract the continuous permittivity profile.

Chapter 4 contains the experimental set-up, an error analysis description, results found from each algorithm, and the accuracy of the two approaches. Conclusions and recommendations for future research are provided in Chapter 5.

II. Discrete Characterization

The purpose of this chapter is to describe the methodology used to develop a discrete permittivity extraction algorithm for an inhomogeneous non-magnetic material. This was accomplished by modeling the material as if it were comprised of piece-wise constant permittivity sections. Figure 2.1 shows how this model works. If one were characterizing a linearly increasing profile, the discrete algorithm would produce a step-like permittivity profile description. The formulation relies on the development presented by Chew [4], Balanis [2], and Havrilla [7].

The basic theory behind the approach is first discussed using a simple two media interface example. The two media example is generalized to represent a stratified media with an arbitrary number of layers. This stratified media example is the foundation for the discrete inhomogeneous approach. This framework is subsequently used to calculate theoretical S_{11} parameters in the permittivity profile algorithm.

Solving for the constitutive parameters algebraically is impossible due to the complexity of the problem. Therefore a root search method is used to solve for the desired permittivities of each section. The root search works by comparing theoretical S_{11} parameters to experimental S_{11} parameters found in the laboratory using the Levenberg-Marquardt numerical method. This is numerical method is used calculate the unknown permittivities of each section within the material, ε_n using

$$\sum_{l=1}^{L} \left| \left[S_{11,l}^{thy}(\omega, \varepsilon_1, \ldots, \varepsilon_N) \right]^2 - \left[S_{11,l}^{\exp}(\omega) \right]^2 \right| < \delta \rightarrow \varepsilon_n .$$

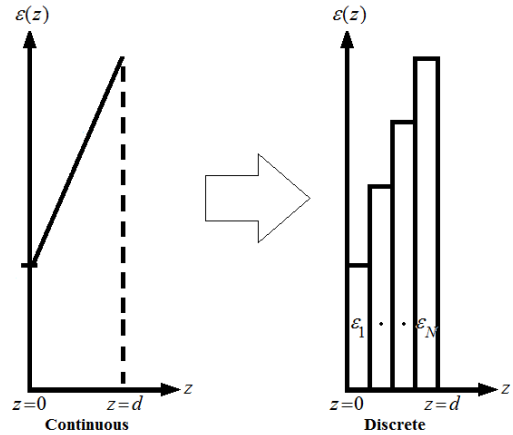

Figure 2.1: Piece-wise constant permittivity profile characterization

In order to find each layers permittivity in this manner, a sufficient number of equations, L, are necessary to create a system of equations that has a greater or equal number of independent solutions for the number of unknowns, N. The approach used to obtain these equations is discussed, including the necessary hardware needed for this purpose. The algorithm is implemented within MatLab code to iteratively calculate the permittivity of each layer so that the difference between the theoretical and experimental values of every S_{11} parameter is minimized to a given tolerance, δ. The Matlab default tolerance was used for this algorithm (10^{-9}).

The discrete approach is advantageous because the underlying theory relies on a much simpler piecewise homogeneous treatment. However, since each layer's permittivity is solved as if it were a distinct media, this requires a large number of independent data points. Despite this drawback, the discrete approach is significantly easier to implement and therefore remains one approach investigated in this study.

2.1 Discrete Theory Development

A single-interface geometry is first discussed before investigating a multi-layered system. In this example two semi-infinite layers are sandwiched together and are placed within a WR-90 waveguide as shown in Figure 2.2.

The first layer is free space with permittivity and permeability of ε_0 and μ_0 respectively, and extends from zero to negative infinity. The second layer has unknown constitutive parameters of ε_1 and μ_1, and extends from zero to positive infinity. An electromagnetic wave is incident upon the material interface at $z = 0$. An artificial boundary denoted by a dotted line exists at $z = d_1$. This will be used to illustrate phase delay as the incident wave passes through the material. At the interface between the two materials, the energy of the wave is partially transmitted through the interface (T_1), or partially reflected by the interface (R_1). Likewise a wave originating from $z=d_1$ would be partially reflected (R_2') and partially transmitted (T_2') through $z = 0$.

The goal of the formulation is to represent the waves b_2 and c_2 at $z=d_1$ in terms of the reflection and transmission of the waves b_1 and c_1 at z=0 in a way that allows material property extraction. After manipulation, the waves will be represented in terms of those found at the front and back interfaces of the material. Note that c_2' and b_2' are simply the waves c_2 and b_2 with a phase shift,

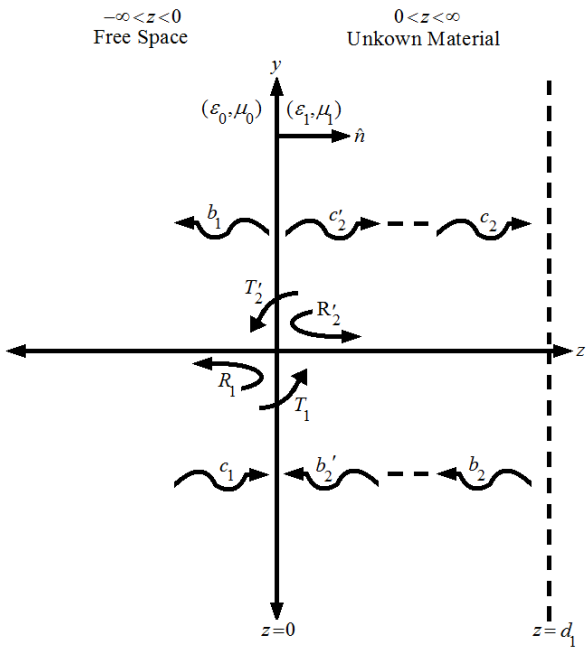

Figure 2.2 Reflection and transmission of waves through a single interface

$$
\begin{aligned}
c_2' &= c_2 e^{jk_{1z}d_1} \\
b_2' &= b_2 e^{-jk_{1z}d_1} \\
k_{1z} &= \sqrt{k_1^2 - k_x^2} \\
k_1 &= \omega\sqrt{\varepsilon_1 \mu_1} \\
k_x &= \left(\frac{\pi}{a}\right),
\end{aligned}
\tag{2.1}
$$

where, k_{1z} is the propagation constant through material one in the z direction, k_x is the propagation constant in the x direction, and k_1 is the propagation constant through the unknown material. Note also that a waveguide geometry is used with a width of a, and that the wave is a TE_{10} mode since this will be the wave excited in the laboratory.

It can be seen from Figure 2.2 that wave b_1, is the sum of the reflection of c_1 and the transmission of b_2'. It also can be seen that c_2' is the sum of the reflection of b_2' and

the transmission of c_1. Using these wave relationships, two equations are written that explicitly define the incoming and outgoing waves at *z=0*

$$\begin{aligned} b_1 &= R_1 c_1 + T_2' b_2' \\ c_2' &= R_2' b_2' + T_1 c_1. \end{aligned} \tag{2.2}$$

Rewriting these equations in a more useful form an expression is obtained

$$\begin{aligned} c_1 &= \frac{1}{T_1} c_2' - \frac{R_2'}{T_1} b_2' \\ b_1 &= \frac{R_1}{T_1} c_2' + (T_2' - \frac{R_1 R_2'}{T_1}) b_2' \end{aligned} \tag{2.3}$$

relating the waves on either side of the boundary.

The reflection coefficients are related to the wave impedances of each layer sharing an interface. In this case layer zero has an impedance of Z_0 and layer one has an impedance of Z_1. The transmission coefficient and reflection coefficients can be written

$$\begin{aligned} R_1 &= -R_2' = \frac{Z_1 - Z_0}{Z_1 + Z_0}, \\ T_1 &= 1 + R_1, \\ T_2' &= 1 + R_2'. \end{aligned} \tag{2.4}$$

Using (2.3) and (2.4) the relations are manipulated to form a matrix equation

$$\begin{bmatrix} c_1 \\ b_1 \end{bmatrix} = \frac{1}{T_1} \begin{bmatrix} 1 & R_1 \\ R_1 & 1 \end{bmatrix} \begin{bmatrix} c_2' \\ b_2' \end{bmatrix}. \tag{2.5}$$

Inserting the relations for c_2' and b_2' from (2.1) into the matrix equation in (2.5), the equation evolves to

$$\begin{bmatrix} c_1 \\ b_1 \end{bmatrix} = \frac{1}{T_1} \begin{bmatrix} e^{jk_{1z}d_1} & R_1 e^{-jk_{1z}d_1} \\ R_1 e^{jk_{1z}d_1} & e^{-jk_{1z}d_1} \end{bmatrix} \begin{bmatrix} c_2 \\ b_2 \end{bmatrix} = \begin{bmatrix} A_{11} & A_{12} \\ A_{21} & A_{22} \end{bmatrix} \begin{bmatrix} c_2 \\ b_2 \end{bmatrix}. \tag{2.6}$$

Here the ***A*** matrix is introduced. Its elements are simplified versions of the matrix on the left of the equation by distributing the transmission term to each element. The ***A*** matrix describes the material characteristics of layer one. This can be seen by looking back to the definition of the propagation constant in (2.1) and recognizing that it is related to the materials permittivity and permeability. Thus a formulation has been found to represent the waves b_2 and c_2 at $z=d_1$ in terms of the reflected and transmitted waves b_1 and c_1 at $z=0$ using the properties of the material.

Now that a simple way of characterizing a single unknown layer has been described, the discussion moves to a development in which there are N arbitrary layers within a material, each with a respective unknown permittivity and permeability. This development is the foundation of the discrete method. Suppose that instead of a two-layer system as in Figure 2.2, there were a multi-layer system as shown in Figure 2.3.

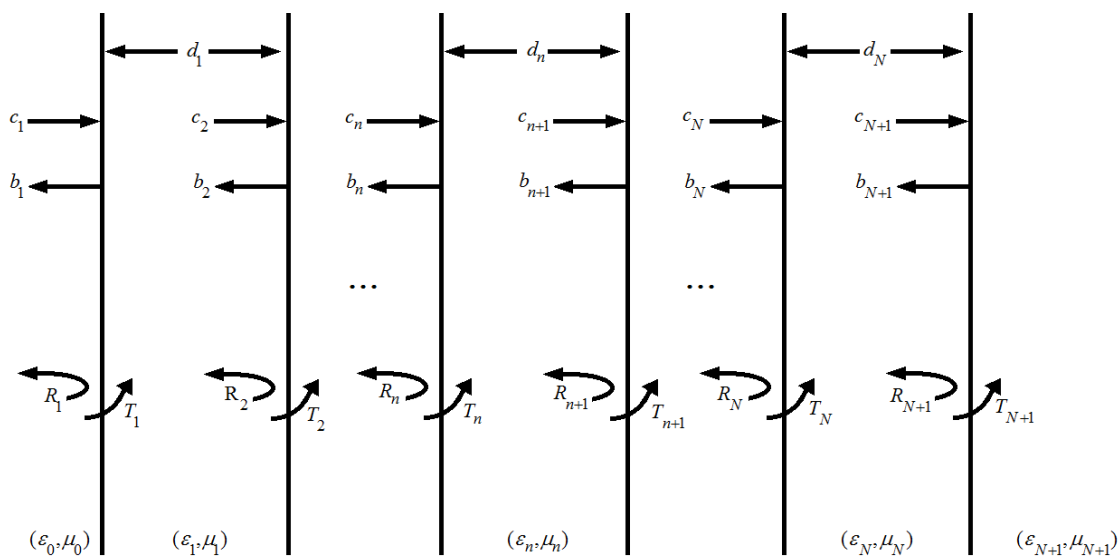

Figure 2.3 Reflection and transmission of waves in a multi-layer system

From this figure a pattern quickly emerges. The problem is generalized with any given layer n with a thickness of d_n, permittivity and permeability of ε_n and μ_n respectively, and applicable waves traveling inside and outside of its left and right interfaces. Also, shown in this figure is the last layer of the material (N), and free space just to the right of the material (N+1).

In the previous example a single interface was investigated to develop an ***A*** matrix that described the waves traveling into and out of an interface containing the desired constitutive parameters. The multi-layer example differs from the single layer example in that now there are ***A*** matrices for each interface. To find the behavior of the entire system one simply needs to take the product of each ***A*** matrix to create an ***A*** matrix for the entire system. This is written as

$$\begin{bmatrix} c_1 \\ b_1 \end{bmatrix} = \prod_{n=1}^{N+1} \frac{1}{T_n} \begin{bmatrix} e^{jk_n d_n} & R_n e^{-jk_n d_n} \\ R_n e^{jk_n d_n} & e^{-jk_n d_n} \end{bmatrix} \begin{bmatrix} c_{N+1} \\ b_{N+1} \end{bmatrix} = \begin{bmatrix} A_{11}^{sys} & A_{12}^{sys} \\ A_{21}^{sys} & A_{22}^{sys} \end{bmatrix} \begin{bmatrix} c_{N+1} \\ b_{N+1} \end{bmatrix}. \tag{2.7}$$

Referring to Figure 2.3 it can be seen that the nth layer has a respective reflection coefficient R_n. The generalized value for this coefficient is

$$R_n = \frac{Z_n - Z_{n-1}}{Z_n + Z_{n-1}} \ , T_n = 1 + R_n. \tag{2.8}$$

This coefficient is related to the wave impedance through the layer Z_n. Also shown in (2.8) is the relationship between the transmission and reflection coefficients at the nth layer.

The wave impedance can be related to the material impedance and propagation constants as seen in

$$Z_n = \frac{\eta_n k_n}{k_{zn}}. \tag{2.9}$$

The material impedance and the propagation constants are then related to the material parameters

$$\begin{aligned} \eta_n &= \sqrt{\frac{\mu_n}{\varepsilon_n}} \\ k_{zn} &= \sqrt{\omega^2 \varepsilon_n \mu_n - k_x} \\ k_n &= \omega \sqrt{\varepsilon_n \mu_n}. \end{aligned} \tag{2.10}$$

The material parameters in these equations allow extraction using a numerical method.

2.2 Constitutive Parameter Extraction

Thus far a characteristic ***A*** matrix for each layer within the material has been developed. This matrix contains a description of how an incident wave will propagate through it. Also shown, was how to combine these ***A*** matrices to produce an ***A*** matrix for the entire system. These descriptions contain the permittivity, permeability and the thickness of each layer. From these relationships the constitutive parameters can be found through a numerical algorithm.

Before this step, the ***A*** matrix for the system must be converted into an ***S*** matrix. This conversion relies on the relationship found in [6]

$$\begin{bmatrix} S_{11} & S_{12} \\ S_{21} & S_{22} \end{bmatrix} = \frac{1}{A_{11}} \begin{bmatrix} A_{21} & A_{11}A_{21} - A_{21}A_{12} \\ 1 & -A_{12} \end{bmatrix}. \tag{2.11}$$

This equation allows the conversion from theoretical *A* parameters to theoretical *S* parameters. This step is required since *S* parameters are measured directly using a network analyzer. With the theoretical *S* parameters and the *S* parameters measured in

the microwave laboratory, there now exists a means to use numerical methods for constitutive parameter extraction.

In order to continue in this manner, there must be sufficient number of independent data points measured in the laboratory. This is accomplished by taking a series of measurements with a short located various distances away from the material. This allows the development of a set of at least N linearly independent solutions for N number of unknowns.

Figure 2.4 illustrates this measurement approach within a waveguide. The inhomogeneous material is located at $z = 0$, and has a thickness of $z=d_N$. As stated earlier it's assumed the material is non-magnetic for the purposes of this thesis.

A fixed short is located a distance l_1 through l_n away from the material depending on the distance measurement. The different distance measurements are achievable by inserting a waveguide shim in between the sample holder and the short. This creates an additional waveguide spacing between the sample and the short, providing a different data point. The hashed lines on the right of Figure 2.4 depict a PEC short which is offset from the sample holder by a given shim length l_n. When calculating the system $\boldsymbol{A}$ matrix for each length measurement, one needs only to update the thickness for the N+1 free space layer by adding the applicable shim length l_n. This allows for the creation of an $\boldsymbol{A}$ matrix for each measurement, which is used to create an S parameter equation for each measurement. From this point, a series of equations each corresponding to a particular shim length is developed to find each layers permittivity.

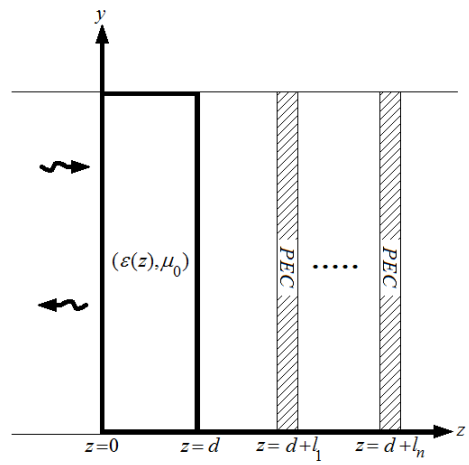

Figure 2.4 Sliding short measurements

These shim lengths were calculated based on the mid-band wavelength. This calculation starts with the relationship between the wavelength and the propagation constant in the *z* direction

$$\lambda_z = \frac{2\pi}{k_z}. \tag{2.12}$$

The propagation constant within the waveguide in the *z* direction is related to the propagation constant in free-space and the waveguide width.

$$k_z = \sqrt{k_0 - \left(\frac{\pi}{a}\right)^2} \tag{2.13}$$

The propagation constant of free-space is related to the frequency and speed of light by the below relation

$$k_0 = \frac{2\pi f}{c}. \tag{2.14}$$

Since the frequency at mid-band, the speed of light in free-space, and the width of the waveguide are known, the wavelength in the z direction can be found. To maintain generality in this discussion, the symbol for this wavelength is kept.

A complete wavelength cycles through a phase of 360 degrees. It is not necessary to include shims through the full cycle. Any measurement beyond a half of a wavelength will not be independent from previous shim measurements. Therefore the shim lengths begin at a phase of zero and up to 180 degrees.

The network analyzer typically needs at least five degrees of phase spacing in order to discern between successive measurements. So to have a confidence in the ability to discern independent measurements, ten degree phase spacing was used in order to calculate the thickness for each shim. The following formula was developed to calculate each shim thickness

$$\frac{n10^0}{360^0} = \frac{l_n}{\lambda_z} \tag{2.15}$$

where l_n is the nth shim thickness, n is the shim number, and λ_z is the mid-band wavelength within the waveguide.

In this way the shim thicknesses were calculated from ten to 180 degrees. A "shim" of zero degrees is not necessary since it would be of zero thickness. A total of eighteen shims were machined. Eighteen shims plus the zero offset produced a total of nineteen possible measurements.

The laboratory data obtained using these shims, and the theoretical formulation found earlier was coded into a root search algorithm using MatLab. The algorithm first

estimates a value for the permittivity of each layer (relative permeability is assumed to be one). These estimates are combined with each layers thickness, d_n, and used to calculate the theoretical ***A*** matrix for each respective layer using the theoretical relations developed earlier. The last layer is of free space and is produced using a respective shim offset. The product of these ***A*** matrices provides a representation for the entire system and represents a particular shim measurement. This procedure is performed in order to produce a system ***A*** matrix for all shim length measurements

$$\varepsilon_n, d_n \rightarrow [A_n], \left[A_{sys}^{thy}\right] = \prod_{n=1}^{N+1} [A_n]. \tag{2.16}$$

The theoretical A parameters are then converted into theoretical S parameters as shown in (2.11)

$$\left[A_{sys}^{thy}\right] \rightarrow \left[S_{sys}^{thy}\right]. \tag{2.17}$$

With the measurement data found in the laboratory, a series of equations are developed using the theoretical S parameters and the experimental S parameters for each shim. These equations are solved simultaneously to find the permittivity of each layer. Since the measurement construct relies on a short, only S_{11} parameters are measured. Each equation in this simultaneous computation takes the form of (2.18). Here l represents the equation created from the corresponding l^{th} shim measurement. Also seen in this equation minimization between the theoretical S_{11} parameter and the experimental S_{11} parameter to a value determined by the tolerance δ

$$\sum_{l=1}^{L} \left| \left[S_{11,l}^{thy}(\omega, \varepsilon_1, ..., \varepsilon_N)\right]^2 - \left[S_{11,l}^{\exp}(\omega)\right]^2 \right| < \delta \rightarrow \varepsilon_n. \tag{2.18}$$

This numerical computation is accomplished using the Levenberg-Marquardt root search method. The details of this algorithm will not be discussed since it would detract from the overall discussion. However, a description of this method can be found in [3]. This root search method is a cross between the Newton method, and the method of steepest descent. First steepest descent is used to refine the estimate to obtain an adequate tolerance, and when sufficient accuracy is acquired the algorithm converges precisely to the solution using the Newton Method.

MatLab has a built-in function that accomplishes this root search called *nlinfit*. A brief description of this function is found in the Matlab help file. Below is a line of code that represents how *nlinfit* is used

beta = nlinfit(X,y,fun,beta0)

where, *beta* is the permittivity solution to the root search, *nlinfit* is the Levenberg-Marquardt root search function, *X* contains the inputs necessary for the function *fun* that are particular to the problem such as frequency and material thickness, *y* is the solution to the theoretical formulation found in the laboratory data, *fun* is the code that contains the theatrical formulation of S_{11}, and *beta0* is the initial constitutive parameter estimate.

An example code using *nlinfit* to calculate constitutive parameters of a single material from two port measurements can be found in *Appendix A*. First, the constants of the geometry are assigned, these are put into the *X* vector. Then the laboratory data is read-in from a text file, this is *y* in the *nlinfit* function and represents the experimental *S* parameters. An initial guess of the permittivity is provided to the Levenberg-Marquardt algorithm using *beta0.* Finally, the algorithm uses *fun* (*Appendix B*) to calculate the

theoretical *S* parameters and compare those to the *S* parameters measured in lab to extract the actual permittivity (*beta*).

2.3 Summary

This chapter discussed a way to characterize layers within a material with theoretical ***A*** matrices. This ***A*** matrix is related to the theoretical *S* parameters. In turn, these theoretical *S* parameters are used with experimental *S* parameters to solve a series of simultaneous equations using the Levenberg-Marquardt algorithm. This allowed the extraction of the permittivity of each layer within the material. In this way a step-like permittivity profile estimate is found for the inhomogeneous material. Before proceeding to the results obtained using this approach, the continuous method is discussed next.

III. Continuous Characterization

This chapter discusses the continuous approach for solving the inhomogeneous permittivity profile. Instead of representing the material as a series of piece-wise constant permittivity layers, this chapter assumes the material to be a continuous linear inhomogeneous profile. Not all profiles of inhomogeneous materials are linear; however, for sufficiently thin materials a linear profile provides a good approximation. This linear approximation also makes it a valid approach for Radar Absorbent Material applications since these are typically thin. A linear profile can be seen from a Taylor series.

$$\varepsilon(z) = \sum_{n=0}^{\infty} \frac{\varepsilon^{(n)}(c)}{n!}(z-c)^n = \varepsilon(c) + \varepsilon'(c)(z-c) + \frac{\varepsilon''(c)(z-c)^2}{2} + \ldots$$

If one were to approximate the function $\varepsilon(z)$ by only using the first and second terms within the series. These two terms would then represent a linear function for an approximate representation of $\varepsilon(z)$ at point c.

Figure 3.1 shows the inhomogeneous material of length d_0 whose profile is solved in this chapter. The graph on the left of the figure shows an incident wave traveling through a free space medium (0), through the material with a linear permittivity profile containing a z-intercept and slope (2), and finally through another region of free space (1). This graph describes the geometry used to calculate S_{11} and S_{21} parameters and for convenience, this geometry will be referred to periodically as the forward measurement. This geometry is investigated first. Next S_{22} and S_{12} parameters are solved using the geometry on the right of Figure 3.1 and are associated with the reverse measurement.

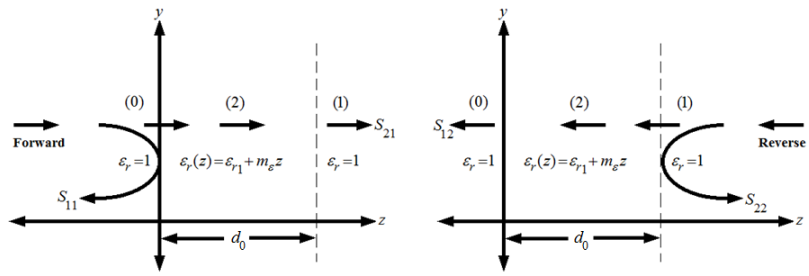

Figure 3.1: Linear inhomogeneous profile with forward and reverse incident waves This graph shows an incident wave traveling through free space (1), then through the inhomogeneous material (2), and finally through additional free space (0).

These theoretical *S* parameters are formulated in this chapter and compared to those measured in the laboratory for permittivity extraction. This extraction is done with the Levenberg-Marquardt algorithm similar to its use in the discrete case. This formulation closely follows the free space development found in [11], except that a wave is propagating within a WR-90 waveguide environment.

3.1 Forward Measurement Field Descriptions

This discussion assumes an incident wave originating from the –*z* direction. The forward transmission and reflection coefficients will contain a subscript *f* to distinguish them from the reverse coefficients developed later in this chapter.

The electric and magnetic fields must be found before constructing theoretical transmission and reflection coefficients. First a formulation for the electric field within region zero is developed. The *y* component of the electric field is a function of the position *x* and *z*. The field's dependence on *z* is denoted by the psi function as shown below

$$E_y(x,z) = \sin(k_x x)\psi(z), \tag{3.1}$$

where, $k_x = \frac{\pi}{a}$.

The electric field in region zero is written directly by inspection. From the figure, forward and reverse traveling waves are expected within the region since there are both incident and reflected waves. For this reason,

$$\psi_0 = R_f e^{jk_z z} + e^{-jk_z z}, \tag{3.2}$$

where, ψ_0 represents the electric field's z dependence for region zero, and k_z is the propagation constant in the z direction. This propagation constant is defined as

$$k_z = \sqrt{k_0^2 - k_x^2}$$
$$k_0 = \omega\sqrt{\varepsilon_0 \mu_0},$$

where, k_x is the x-directed wavenumber, k_0 is the free space wavenumber, and a denotes waveguide width.

There is only a transmitted wave ψ_1 in region one. So this is also written by inspection

$$\psi_1 = T_f e^{jk_z(d_0 - z)}. \tag{3.3}$$

Now that the electric fields for region zero and one are solved, the magnetic fields are found easily from Faraday's Law

$$H_{x0}(x,z) = \sin(k_x x)\frac{j}{\omega\mu_0}\frac{d\psi_0}{dz}. \tag{3.4}$$

Although there is also a z component of the magnetic field, it is not needed for enforcement of boundary conditions, and therefore only the x component of the magnetic is used. The magnetic field for region zero simplifies to

$$H_{x0}(x,z) = \sin(k_x x)\frac{k_z}{\omega\mu_0}\left[e^{-jk_z z} - R_f e^{jk_z z}\right]. \tag{3.5}$$

Using this same procedure the x component of the magnetic field for region one is

$$H_{x1} = (x,z) = \sin(k_x x)\frac{k_z}{\omega\mu_0}T_f e^{jk_z(d_0 - z)}. \tag{3.6}$$

The process to find the electric and magnetic fields for region two is more involved since the region is inhomogeneous. A differential equation is derived from Maxwell's equations in order to describe the electric fields in region two.

Faraday's law shows that the electric field will circulate around a magnetic field, and Ampere's Law shows that a magnetic field will circulate around an electric field

$$\begin{aligned} \nabla \times \vec{E} &= -j\omega\mu\vec{H} \\ \nabla \times \vec{H} &= j\omega\varepsilon\vec{E}. \end{aligned} \tag{3.7}$$

In these equations $\vec{E}$ represents the electric field, $\vec{H}$ the magnetic field, ε and μ the permittivity and permeability, and ω represents the angular frequency of the wave.

Expanding the curl operator and recognizing y invariance since the material properties do not change in the y direction, Faraday's law yields

$$-\hat{x}\frac{\partial E_y}{\partial z} + \hat{y}\left(\frac{\partial E_x}{\partial z} - \frac{\partial E_z}{\partial x}\right) + \hat{z}\left(\frac{\partial E_y}{\partial x}\right) = -j\omega\mu(\hat{x}H_x + \hat{y}H_y + \hat{z}H_z). \tag{3.8}$$

By equating the vector components a set of three equations results

$$\begin{aligned} \frac{\partial E_y}{\partial z} &= j\omega\mu H_x && E_y, H_x : \mathrm{TE}^z \\ \frac{\partial E_z}{\partial x} - \frac{\partial E_x}{\partial z} &= j\omega\mu H_y && E_z, E_x, H_x : \mathrm{TM}^z \\ \frac{\partial E_y}{\partial x} &= -j\omega\mu H_z. && E_y, H_z : \mathrm{TE}^z \end{aligned} \tag{3.9}$$

Ampere's law results in a similar formulation

$$-\hat{x}\frac{\partial H_y}{\partial z}+\hat{y}\left(\frac{\partial H_x}{\partial z}-\frac{\partial H_z}{\partial x}\right)+\hat{z}\left(\frac{\partial H_y}{\partial x}\right)=j\omega\varepsilon(\hat{x}E_x+\hat{y}E_y+\hat{z}E_z). \qquad (3.10)$$

Again, a set of three equations is found by equating the vector components from (3.10)

$$\begin{aligned}
&\frac{\partial H_y}{\partial z}=-j\omega\varepsilon E_x && E_x, H_y : \mathrm{TM}^z \\
&\frac{\partial H_z}{\partial x}-\frac{\partial H_x}{\partial z}=-j\omega\varepsilon E_y && E_y, H_x, H_z : \mathrm{TE}^z \\
&\frac{\partial H_y}{\partial x}=j\omega\varepsilon E_z. && E_z, H_y : \mathrm{TM}^z
\end{aligned} \qquad (3.11)$$

These results make physical sense because in the TE_z case the magnetic field circulates around the electric field, and in the TM_z case the electric field circulates around the magnetic field.

The problem geometry dictates *y* invariance. This means that the equations are decoupled, and a TE_z excitation will not couple into a TM_z field set. This simplifies the problem considerably because the TE_z field excited in lab will not generate TM_z fields. As a result only TE_z waves are required in this analysis.

In particular the problem will consist of the TE_{10}^z mode, since this specific mode will be used within the waveguide. Figure 3.2 shows the expected waves within the guide.

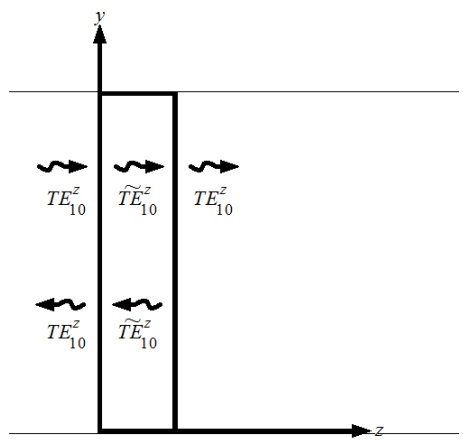

Figure 3.2: TE_{10} modes in WR-90 waveguide

Solving the TE_z equations from (3.9) in terms of H_x and H_z, and inserting them into the second equation in (3.11), a partial differential equation in terms of the electric field is derived

$$\frac{\partial^2 E_y}{\partial x^2} + \frac{\partial^2 E_y}{\partial z^2} + k^2(z)E_y = 0. \tag{3.12}$$

This is a homogeneous partial differential equation that represents the electric field in the inhomogeneous material. Note that electric field E_y is a function of x and z for region two and is written

$$E_y(x,z) = \sin(k_x x)\psi_2(z). \tag{3.13}$$

By assuming separation of variables (3.12) is reduced to simple derivatives

$$-k_x^2 E_y + \frac{d^2 E_y}{dz^2} + k^2(z)E_y = 0. \tag{3.14}$$

Note that the partial double derivative of E_y with respect to x is just $-k_x^2 E_y$ since there are only standing waves in the waveguide along the x-axis.

This result simplifies further using

$$k^2 = k_x^2 + k_z^2 \tag{3.15}$$

to obtain

$$\frac{d^2 E_y}{dz^2} + k_z^2(z) E_y = 0. \tag{3.16}$$

Where, k_z is functionally dependent on position z because the material is inhomogeneous in this direction, and k_y is zero since the material is y invariant.

There is no general analytic solution to this differential equation so a particular profile is assumed. For sufficiently thin materials a linear profile can be assumed without losing significant accuracy. This assumption dictates a linear propagation constant

$$k_z^2(z) = k^2(z) - k_x^2 = \omega^2 \varepsilon_0 \mu_0 \varepsilon_r(z) - k_x^2 \tag{3.17}$$

This simplifies further into a more useful representation

$$k_0^2 \varepsilon_r(z) - k_x^2 = k_0^2 (\varepsilon_{r1} + m_\varepsilon z - \frac{k_x^2}{k_0^2}). \tag{3.18}$$

From (3.18) the permittivity profile is much easier to discern. By factoring out the propagation constant of free space the equation is left with the relative permittivity intercept ε_{r1} and the relative permittivity slope m_ε of the inhomogeneous profile. If the slope were to go to zero, the resulting equation would be exactly equal to that for a homogeneous material. Substituting (3.18) into the propagation term in (3.16) yields

$$\left\{ \frac{d^2}{dz^2} + k_0^2 [\varepsilon_{r1} + m_\varepsilon z - \frac{k_x^2}{k_0^2}] \right\} \psi_2(z) = 0 \tag{3.19}$$

where, the notation used for the electric field in region two is Ψ_2.

The differential equation in (3.19) is in a complicated form. A change of variables is used to simplify the problem

$$\eta = \left(\frac{k_0}{m_\varepsilon}\right)^{2/3}\left[m_\varepsilon z + \varepsilon_{r1} - \frac{k_x^2}{k_0^2}\right], \tag{3.20}$$

or equivalently,

$$z = \frac{1}{m_\varepsilon}\left[\left(\frac{m_\varepsilon}{k_0}\right)^{2/3}\eta - \left(\varepsilon_{r1} - \frac{k_x^2}{k_0^2}\right)\right]. \tag{3.21}$$

One could substitute the double derivative with respect to z with the double derivative with respect to η by knowing

$$\frac{d\psi_2(z)}{dz} = \frac{d\psi_2(\eta)}{d\eta}\frac{d\eta}{dz}, \tag{3.22}$$

and

$$\frac{d^2\psi_2(z)}{dz^2} = \frac{d}{d\eta}\left[\frac{d\psi_2(z)}{dz}\right]\frac{d\eta}{dz}. \tag{3.23}$$

The derivative of η with respect to z is

$$\frac{d\eta}{dz} = m_\varepsilon^{1/3}k_0^{2/3}, \tag{3.24}$$

so that (3.19) becomes

$$\left(\frac{d^2}{d\eta^2}\left(m_\varepsilon^{1/3}k_0^{2/3}\right)^2 + k_0^2[\varepsilon_{r1} + m_\varepsilon\left\{\frac{1}{m_\varepsilon}\left[\left(\frac{m_\varepsilon}{k_0}\right)^{2/3}\eta - \left(\varepsilon_{r1} - \frac{k_x^2}{k_0^2}\right)\right]\right\} - \frac{k_x^2}{k_0^2}]\right)\psi_2(\eta) = 0. \tag{3.25}$$

Simplifying this expression results in the differential equation

$$\left[\frac{d^2}{d\eta^2} + \eta\right]\psi_2(\eta) = 0. \tag{3.26}$$

The solution to this differential equation is found using the Frobenius method. One will find the solution to be the scaled sum of two fractional-order Bessel functions as seen in [10]

$$\psi_2(w) = w^{1/3}\left[AJ_{1/3}(w) + BY_{1/3}(w)\right], \tag{3.27}$$

where, A and B are constants, and an additional change of variables was made

$$w = \frac{2}{3}\eta^{3/2},$$
$$w = \frac{2}{3}\left(\frac{k_0}{m_\varepsilon}\right)(m_\varepsilon z + \varepsilon_{r1} - \frac{k_x^2}{k_0^2})^{3/2}.$$

Bessel functions make physical sense, since the waves traveling forward and backward should appear sinusoidal. Also, one would expect the waves to diminish in amplitude and decrease in wavelength as they travel through the material to account for loss and changing permittivity within the material. This phenomenon can be seen from the relationship

$$\lambda = \frac{v}{f} = \frac{c}{f\sqrt{\varepsilon\mu}},$$

where v and f are the velocity and frequency of the wave respectively, and c is the speed of light in free space. As permittivity increases the wavelength would naturally decrease. Since these relationships intuitively represent what is expected in the problem, the solution in (3.27) is reasonable and the formulation continuous to finding the magnetic field in region two.

The magnetic field can be found as previously accomplished using Faraday's Law. In this case, a change of variables was introduced, and therefore the derivative of w with respect to z must be added to the equation

$$H_{x2}(x,z) = \sin(k_x x)\frac{j}{\omega\mu_0}\frac{d\psi_2}{dw}\frac{dw}{dz}. \tag{3.28}$$

Using the property of Bessel functions below, taking the derivative of the electric field becomes quite simple

$$\frac{d}{dz}\left[z^{\nu}\xi_{\nu}(z)\right] = z^{\nu}\xi_{\nu-1}(z).$$

This holds true for any Bessel function $\xi_{\nu}(z)$. Using this equation the derivative of the electric field is

$$\frac{d\psi_2}{dw} = w^{1/3}\left[AJ_{-2/3}(w) + BY_{-2/3}(w)\right]. \tag{3.29}$$

The derivative of w with respect to z is

$$\frac{dw}{dz} = k_0\left(m_{\varepsilon}z + \varepsilon_{r1} - \frac{k_x^2}{k_0^2})\right)^{1/2}. \tag{3.30}$$

Using (3.29) and (3.30) the magnetic field for region two becomes

$$H_{x2}(x,z) = \sin(k_x x)\frac{j}{\omega\mu_0}k_0 w^{1/3}\left(m_{\varepsilon}z + \varepsilon_{r1} - \frac{k_x^2}{k_0^2}\right)^{1/2}\left[AJ_{-2/3}(w) + BY_{-2/3}(w)\right]. \tag{3.31}$$

Now that both the electric and magnetic fields in all regions are known, boundary conditions are applied to find the forward measurement's reflection and transmission coefficients.

3.2 Forward Measurement Transmission & Reflection Coefficients

Since the tangential electric field components are continuous across the boundary at *z=0*, the electric field in region zero and region two must be equal

$$\psi_0(0) = \psi_2(0). \tag{3.32}$$

Note that the electric fields *x* dependence cancels and only the *z* dependent term remains. This cancelation will occur when applying all boundary conditions including those for the magnetic fields. Using the equations for the electric fields in regions zero and two, and evaluating at *z=0*, results in

$$\begin{aligned} \psi_0(0) &= R_f + 1 \\ \psi_2(0) &= w_0^{1/3}\left[AJ_{1/3}(w_0) + BY_{1/3}(w_0)\right]. \end{aligned} \tag{3.33}$$

Equating these two fields at the boundary yields

$$1 + R_f = w_0^{1/3}\left[AJ_{1/3}(w_0) + BY_{1/3}(w_0)\right], \tag{3.34}$$

where,

$$w_0 = \frac{2}{3}\left(\frac{k_0}{m_\varepsilon}\right)\left(\varepsilon_{r1} - \frac{k_x^2}{k_0^2}\right)^{3/2}.$$

The next boundary is $z = d_0$ in which the electric fields are equal in regions one and two

$$\psi_1(d_0) = \psi_2(d_0). \tag{3.35}$$

At this boundary the electric fields for both regions are

$$\begin{aligned} \psi_1(d_0) &= T_f \\ \psi_2(d_0) &= w_1^{1/3}\left[AJ_{1/3}(w_1) + BY_{1/3}(w_1)\right], \end{aligned} \tag{3.36}$$

where,

$$w_1 = \frac{2}{3}\left(\frac{k_0}{m_\varepsilon}\right)\left(m_\varepsilon d_0 + \varepsilon_{r1} - \frac{k_x^2}{k_0^2}\right)^{3/2}$$

Equating these tangential electric field values according to (3.35) yields

$$T_f = w_1^{1/3}\left[AJ_{1/3}(w_1) + BY_{1/3}(w_1)\right]. \tag{3.37}$$

Next the boundary conditions for the magnetic fields are applied, starting with the continuity of tangential magnetic fields across regions zero and two using $z = 0$

$$H_{x0}(0) = H_{x2}(0). \tag{3.38}$$

Equating the two formulations at this boundary the following equation results

$$1 - R_f = \frac{jk_0 w_0^{1/3}}{k_z}\left(\varepsilon_{r1} - \frac{k_x^2}{k_0^2}\right)^{1/2}\left[AJ_{-2/3}(w_0) + BY_{-2/3}(w_0)\right]. \tag{3.39}$$

Finally, the continuity of the magnetic field across regions one and two at $z = d_0$ is applied

$$H_{x1}(d_0) = H_{x2}(d_0). \tag{3.40}$$

Using this boundary condition and the equation for the magnetic field in region two developed earlier (3.30) the last of the four boundary value equations for the forward case is found

$$T_f = \frac{jk_0 w_1^{1/3}}{k_z}\left(m_\varepsilon d_0 + \varepsilon_{r1} - \frac{k_x^2}{k_0^2}\right)^{1/2}\left[AJ_{-2/3}(w_1) + BY_{-2/3}(w_1)\right]. \tag{3.41}$$

At this point four equations have been developed from the boundary conditions. These equations define the reflection and transmission coefficients for the forward case.

Note that the constants A and B must be removed by solving these equations simultaneously

$$\begin{aligned}
1+R_f &= w_0^{1/3}\left[AJ_{1/3}(w_0)+BY_{1/3}(w_0)\right],\\
T_f &= w_1^{1/3}\left[AJ_{1/3}(w_1)+BY_{1/3}(w_1)\right],\\
1-R_f &= jC_{1f}w_0^{1/3}\left[AJ_{-2/3}(w_0)+BY_{-2/3}(w_0)\right],\\
T_f &= jC_{2f}w_1^{1/3}\left[AJ_{-2/3}(w_1)+BY_{-2/3}(w_1)\right],
\end{aligned} \tag{3.42}$$

where,

$$\begin{aligned}
C_{1f} &= \frac{k_0}{k_z}(\varepsilon_{r1}-\frac{k_x^2}{k_0^2})^{1/2},\\
C_{2f} &= \frac{k_0}{k_z}(m_\varepsilon d_0+\varepsilon_{r1}-\frac{k_x^2}{k_0^2})^{1/2}.
\end{aligned}$$

Transmission and reflection coefficient equations are found by solving the set of relations in (3.42). The coefficients are again labeled with a subscript *f* to emphasize that they are for the forward measurement; those taken by an incident wave originating from the –*z* direction

$$T_f = 2\left(\frac{w_1}{w_0}\right)^{1/3}\left[\frac{N_{1f}+N_{2f}}{D_{1f}D_{2f}+D_{3f}D_{4f}}\right], \tag{3.43}$$

$$R_f = 2\left[\frac{N_{3f}+N_{4f}}{D_{1f}D_{2f}+D_{3f}D_{4f}}\right]-1, \tag{3.44}$$

where,

$$
\begin{aligned}
N_{1f} &= J_{1/3}(w_1)\left[Y_{1/3}(w_1) - jC_{2f}Y_{-2/3}(w_1)\right] \\
N_{2f} &= Y_{1/3}(w_1)\left[jC_{2f}J_{-2/3}(w_1) - J_{1/3}(w_1)\right] \\
N_{3f} &= J_{1/3}(w_0)\left[Y_{1/3}(w_1) - jC_{2f}Y_{-2/3}(w_1)\right] \\
N_{4f} &= Y_{1/3}(w_0)\left[jC_{2f}J_{-2/3}(w_1) - J_{1/3}(w_1)\right] \\
D_{1f} &= \left[Y_{1/3}(w_1) - jC_{2f}Y_{-2/3}(w_1)\right] \\
D_{2f} &= \left[jC_{1f}J_{-2/3}(w_0) + J_{1/3}(w_0)\right] \\
D_{3f} &= \left[Y_{1/3}(w_0) + jC_{1f}Y_{-2/3}(w_0)\right] \\
D_{4f} &= \left[jC_{2f}J_{-2/3}(w_1) - J_{1/3}(w_1)\right].
\end{aligned}
$$

Fortunately the solution for the transmission coefficient can be reduced using the relationship for any Bessel function ξ_ν,

$$\frac{d}{dz}\left[\xi_\nu(\alpha z)\right] = -\alpha\xi_{\nu+1}(\alpha z) + \frac{\nu}{z}\xi_\nu(\alpha z), \tag{3.45}$$

and the identity,

$$J_\nu(z)Y_\nu'(z) - Y_\nu(z)J_\nu'(z) = \frac{2}{\pi z}, \tag{3.46}$$

which is also known as the Wronskian. This allows the transmission coefficient to reduce

$$T_f = \left(\frac{-4jC_{2f}}{\pi(w_1^2 w_0)^{1/3}}\right)\left[D_{1f}D_{2f} + D_{3f}D_{4f}\right]^{-1}. \tag{3.47}$$

There were no such simplifications that could be made for the denominator term or for the numerator for the reflection coefficient and therefore the form shown in (3.44) remains.

The transmission and reflection coefficients are related to S parameters as shown below

$$\begin{aligned} S_{11}^{thy}(\omega, \varepsilon_{r1}, m_{\varepsilon}) &= R_f(\omega, \varepsilon_{r1}, m_{\varepsilon}) \\ S_{21}^{thy}(\omega, \varepsilon_{r1}, m_{\varepsilon}) &= T_f(\omega, \varepsilon_{r1}, m_{\varepsilon}). \end{aligned} \tag{3.48}$$

Next the theoretical S parameters for the reverse measurement are developed.

3.3 Reverse Measurement Field Descriptions

The development in this section closely follows the approach used in section 3.1. In this section however, the wave originates in the z direction, as shown in Figure 3.3. The reflection and transmission coefficients belong to the reverse measurement set and are denoted with a subscript r. These coefficients are directly related to the S_{22} and S_{12} scattering parameters.

The formulation begins with finding the electric field within region zero. Using the same convention for the electric field, ψ_0 can be written by inspection as

$$\psi_0 = T_r e^{jk_z z}. \tag{3.49}$$

A reflected wave and an incident wave will be present in region one so that ψ_1 is

$$\psi_1 = e^{-jk_z(d_0 - z)} + R_r e^{jk_z(d_0 - z)}. \tag{3.50}$$

Now that the electric fields are known for regions zero and one, the magnetic fields are found from Faraday's law

$$H_{x0}(x,z) = \sin(k_x x)\frac{j}{\omega\mu_0}\frac{d\psi_0}{dz}. \tag{3.51}$$

Therefore the magnetic field for region zero is

$$H_{x0}(x,z) = \sin(k_x x)\frac{-k_z}{\omega\mu_0}T_r e^{jk_z z}. \tag{3.52}$$

In a similar fashion the magnetic field for region one is

$$H_{x1}(x,z) = \sin(k_x x)\frac{k_z}{\omega\mu_0}\left[R_r e^{jk_z(d_0-z)} - e^{-jk_z(d_0-z)}\right]. \tag{3.53}$$

At this point the electric fields and magnetic fields have been found for region zero and one. For region two, no additional formulation is needed since the wave within this region will behave similarly whether the incident wave originates from the *–z* or *z* direction. For this reason, (3.27) and (3.31) can be also used in the reverse development.

3.4 Reverse Measurement Transmission & Reflection Coefficients

The tangential electric field is continuous across the boundary *z=0*. Because of this, the electric field in region zero is equal to the electric field in region two as noted in (3.32). At this boundary the *z* dependence of the electric fields for region zero and region two are

$$\begin{aligned} \psi_0(0) &= T_r \\ \psi_2(0) &= w_0^{1/3}\left[AJ_{1/3}(w_0) + BY_{1/3}(w_0)\right]. \end{aligned} \tag{3.54}$$

Note that w_0 is equivalent to that introduced for the forward case. Equating these two electric fields results in

$$T_r = w_0^{1/3}\left[AJ_{1/3}(w_0) + BY_{1/3}(w_0)\right]. \tag{3.55}$$

Next, the boundary condition for $z=d_0$ is applied. Here the tangential electric fields are equal for regions one and two. The fields for the two regions are shown below

$$\begin{aligned} \psi_1(d_0) &= 1 + R_r \\ \psi_2(d_0) &= w_1^{1/3}\left[AJ_{1/3}(w_1) + BY_{1/3}(w_1)\right]. \end{aligned} \tag{3.56}$$

Note again that w_1 was defined earlier in (3.36). Equating these two electric fields results in the relation

$$1 + R_r = w_1^{1/3}\left[AJ_{1/3}(w_1) + BY_{1/3}(w_1)\right]. \tag{3.57}$$

Next boundary conditions are used to find two additional equations from the continuity of tangential magnetic fields. This development starts with the magnetic fields across regions zero and two at $z = 0$. At this boundary the magnetic fields are

$$\begin{aligned} H_{x0}(x,0) &= \sin(k_x x)\frac{-k_z T_r}{\omega\mu_0} \\ H_{x2}(x,0) &= \sin(k_x x)\frac{jk_0 w_0^{1/3}}{\omega\mu_0}\left(\varepsilon_{r1} - \frac{k_x^2}{k_0^2}\right)^{1/2}\left[AJ_{-2/3}(w_0) + BY_{-2/3}(w_0)\right]. \end{aligned} \tag{3.58}$$

Equating these two magnetic fields across the boundary a third equation results

$$T_r = \frac{-jk_0 w_0^{1/3}}{k_z}\left(\varepsilon_{r1} - \frac{k_x^2}{k_0^2}\right)^{1/2}\left[AJ_{-2/3}(w_0) + BY_{-2/3}(w_0)\right]. \tag{3.59}$$

Finally, the magnetic fields across the boundary $z=d_0$ are also equal. These magnetic fields are

$$\begin{aligned} H_{x1}(x,d_0) &= \sin(k_x x)\frac{k_z}{\omega\mu_0}\left(R_r - 1\right) \\ H_{x2}(x,d_0) &= \sin(k_x x)\frac{jk_0 w_1^{1/3}}{\omega\mu_0}\left(m_\varepsilon d_0 + \varepsilon_{r1} - \frac{k_x^2}{k_0^2}\right)^{1/2}\left[AJ_{-2/3}(w_1) + BY_{-2/3}(w_1)\right]. \end{aligned} \tag{3.60}$$

This results in the last equation

$$R_r - 1 = \frac{jk_0 w_1^{1/3}}{k_z}\left(m_\varepsilon d_0 + \varepsilon_{r1} - \frac{k_x^2}{k_0^2}\right)^{1/2}\left[AJ_{-2/3}(w_1) + BY_{-2/3}(w_1)\right]. \tag{3.61}$$

The four equations describing the transmission and reflection coefficients for the reverse measurement are written as

$$
\begin{aligned}
T_r &= w_0^{1/3}\left[AJ_{1/3}(w_0)+BY_{1/3}(w_0)\right] \\
1+R_r &= w_1^{1/3}\left[AJ_{1/3}(w_1)+BY_{1/3}(w_1)\right] \\
T_r &= jC_{1r}w_0^{1/3}\left[AJ_{-2/3}(w_0)+BY_{-2/3}(w_0)\right] \\
R_r-1 &= jC_{2r}w_1^{1/3}\left[AJ_{-2/3}(w_1)+BY_{-2/3}(w_1)\right]
\end{aligned}
\tag{3.62}
$$

where,

$$
\begin{aligned}
C_{1r} &= -\frac{k_0}{k_z}(\varepsilon_{r1}-\frac{k_x^2}{k_0^2})^{1/2} \\
C_{2r} &= \frac{k_0}{k_z}(m_\varepsilon d_0+\varepsilon_{r1}-\frac{k_x^2}{k_0^2})^{1/2}.
\end{aligned}
$$

With some algebra the constants A and B drop out and relations for the transmission and reflection coefficients are

$$
T_r = 2\left(\frac{w_0}{w_1}\right)^{1/3}\left[\frac{N_{1r}+N_{2r}}{D_{1r}D_{2r}+D_{3r}D_{4r}}\right], \tag{3.63}
$$

$$
R_r = 2\left[\frac{N_{3r}+N_{4r}}{D_{1r}D_{2r}+D_{3r}D_{4r}}\right]-1, \tag{3.64}
$$

where,

$$
\begin{aligned}
N_{1r} &= J_{1/3}(w_0)\left[Y_{1/3}(w_0)-jC_{1r}Y_{-2/3}(w_0)\right] \\
N_{2r} &= Y_{1/3}(w_0)\left[jC_{1r}J_{-2/3}(w_0)-J_{1/3}(w_0)\right] \\
N_{3r} &= J_{1/3}(w_1)\left[Y_{1/3}(w_0)-jC_{1r}Y_{-2/3}(w_0)\right] \\
N_{4r} &= Y_{1/3}(w_1)\left[jC_{1r}J_{-2/3}(w_0)-J_{1/3}(w_0)\right] \\
D_{1r} &= \left[Y_{1/3}(w_1)-jC_{2r}Y_{-2/3}(w_1)\right] \\
D_{2r} &= \left[jC_{1r}J_{-2/3}(w_0)-J_{1/3}(w_0)\right] \\
D_{3r} &= \left[Y_{1/3}(w_0)-jC_{1r}Y_{-2/3}(w_0)\right] \\
D_{4r} &= \left[J_{1/3}(w_1)-jC_{2r}J_{-2/3}(w_1)\right]
\end{aligned}
$$

As done for the forward case, the transmission coefficient can be further simplified using (3.45) and (3.46) to yield

$$T_r = \left(\frac{-4jC_{1r}}{\pi (w_0^2 w_1)^{1/3}} \right) \left[D_{1r} D_{2r} + D_{3r} D_{4r} \right]^{-1}. \tag{3.65}$$

Now that the reflection and transmission coefficients are found for the reverse measurement, the associated theoretical S parameters are simply

$$\begin{aligned} S_{22}^{thy}(\omega, \varepsilon_{r1}, m_\varepsilon) &= R_r(\omega, \varepsilon_{r1}, m_\varepsilon) \\ S_{12}^{thy}(\omega, \varepsilon_{r1}, m_\varepsilon) &= T_r(\omega, \varepsilon_{r1}, m_\varepsilon). \end{aligned} \tag{3.66}$$

3.5 Numerical Computations of Slope and Intercept

To summarize, the four transmission and reflection coefficients are related directly to S parameters as shown below

$$\begin{aligned} T_f(\omega, \varepsilon_{r1}, m_\varepsilon) &= S_{21}^{thy}(\omega, \varepsilon_{r1}, m_\varepsilon) \\ R_f(\omega, \varepsilon_{r1}, m_\varepsilon) &= S_{11}^{thy}(\omega, \varepsilon_{r1}, m_\varepsilon) \\ T_r(\omega, \varepsilon_{r1}, m_\varepsilon) &= S_{12}^{thy}(\omega, \varepsilon_{r1}, m_\varepsilon) \\ R_r(\omega, \varepsilon_{r1}, m_\varepsilon) &= S_{22}^{thy}(\omega, \varepsilon_{r1}, m_\varepsilon). \end{aligned}$$

Before continuing, a quick check is done to see if the mathematical representation of scattering parameters reflects physically expected results. This allows a check on the accuracy of the formulations. Unfortunately, allowing the slope m_ε to go to zero to verify the solution reduces to a homogeneous relationship does not result in a useful test. This is because as m_ε approaches zero, fields would become infinite within the inhomogeneous region. Even taking the Bessel functions to their asymptotic approximations did not allow for a testable result.

However, some other checks can be made. Since the inhomogeneous profile is asymmetric, the equations for the forward and reverse reflection coefficients should not be equal. Referring back to (3.44) and (3.46) it is apparent that these coefficients indeed

differ. The theorem applying to linear and isotropic materials can be used. For both homogeneous and inhomogeneous materials reciprocity signifies that the forward and reverse transmission coefficients should be equal. Referring back to (3.47) and (3.65) it is seen after inserting the values for C_{1f}, C_{2f}, C_{1r}, C_{2r}, w_0, and w_1, that these transmission coefficients are indeed equal. This provides reasonable confidence that these scattering parameter formulations are accurate.

The four scattering parameter equations are solved using the Levenberg-Marquardt algorithm to find the relative permittivity z-intercept and slope within the inhomogeneous material

$$\sum_i \left| \left[S_i^{thy}(\omega, \varepsilon_{r1}, m_\varepsilon) \right]^2 - \left[S_i^{\exp}(\omega) \right]^2 \right| < \delta \rightarrow \varepsilon_{r1}, m_\varepsilon, \tag{3.67}$$

where the scattering parameters are indicted using i=21,11,12, and 22.

3.6 Summary

In this chapter theoretical scattering parameters were solved allowing a linear permittivity profile extraction. This was accomplished by splitting the geometry up into three regions: zero and one of homogeneous free-space, and the second of an inhomogeneous material. From this point, boundary conditions were applied to solve for the forward and reverse incident wave's reflection and transmission coefficients. These coefficients were directly related to the scattering parameters.

Finally, as done in the discrete case, an algorithm was developed via MatLab to numerically solve for the linear profile using the Levenberg-Marquardt algorithm with experimentally captured scattering parameters.

IV. Analysis & Results

This chapter discusses the steps taken in the laboratory to capture data, and the results from the discrete and continuous permittivity profile algorithms. A short error analysis section shows how permittivity profile uncertainty was calculated. All results are presented using Matlab plots to clearly show the accuracy of each algorithm in various testing scenarios. Also included in this chapter is a comparison between both approaches and a discussion of advantages and disadvantages of each.

A description of the equipment used, the materials tested, and the measurements taken are included for completeness of the discussion. The discrete algorithm required a significant number of measurements, and so details on data gathering are included for this approach. The continuous approach required only one measurement, and so only a brief description is required.

This chapter begins with the experimental set up, the calibration and measurement procedures, error sources, algorithm results, and concludes with a summary.

4.1 Experimental Set Up

The scattering parameters were measured using the Agilent Technologies Network Analyzer shown in Figure 4.1. Shown is the *S* Parameter measurement screen, the two ports that connect to the waveguide, and the keypad.

Several waveguide parts were needed to collect the necessary data. Shown in Figure 4.2 are the short (A), the sample holder (B), and material samples, including Plexiglas (C) and Mica (D).

Figure 4.3 shows a picture of the shims displaying their thicknesses, which were calculated earlier. Starting from top to bottom, and going from left to right, the shims get progressively smaller. The last shim shows the face of each offset. In table 4.1 the specific thicknesses of each shim is listed.

Finally, Figure 4.4 and Figure 4.5 show the experimental set up for the discrete and continuous measurements, respectively. Figure 4.4 shows the coaxial cable (A) that connects the network analyzer to the waveguide (B), the sample holder (C), the shim used for the applicable measurement (D), and the short (E). Note also in this figure that only measurements were taken in the discrete case using one port (S_{11}). Figure 4.5 shows a slightly different set up. In this figure measurements were taken using two ports (S_{11}, S_{21}, S_{12}, S_{22}), both labeled A, where the left was port one, and the right was port two. The waveguide is also shown (B) along with the sample holder (C).

Table 4.1: Shim thickness measurements

Shim	A	B	C	D	E	F	G	H	I
Thickness (mm)	19.87	18.76	17.60	16.54	15.43	14.34	13.23	12.10	11.02
Shim	J	K	L	M	N	O	P	Q	R
Thickness (mm)	9.96	8.79	7.71	6.61	5.52	4.40	3.31	2.19	1.10

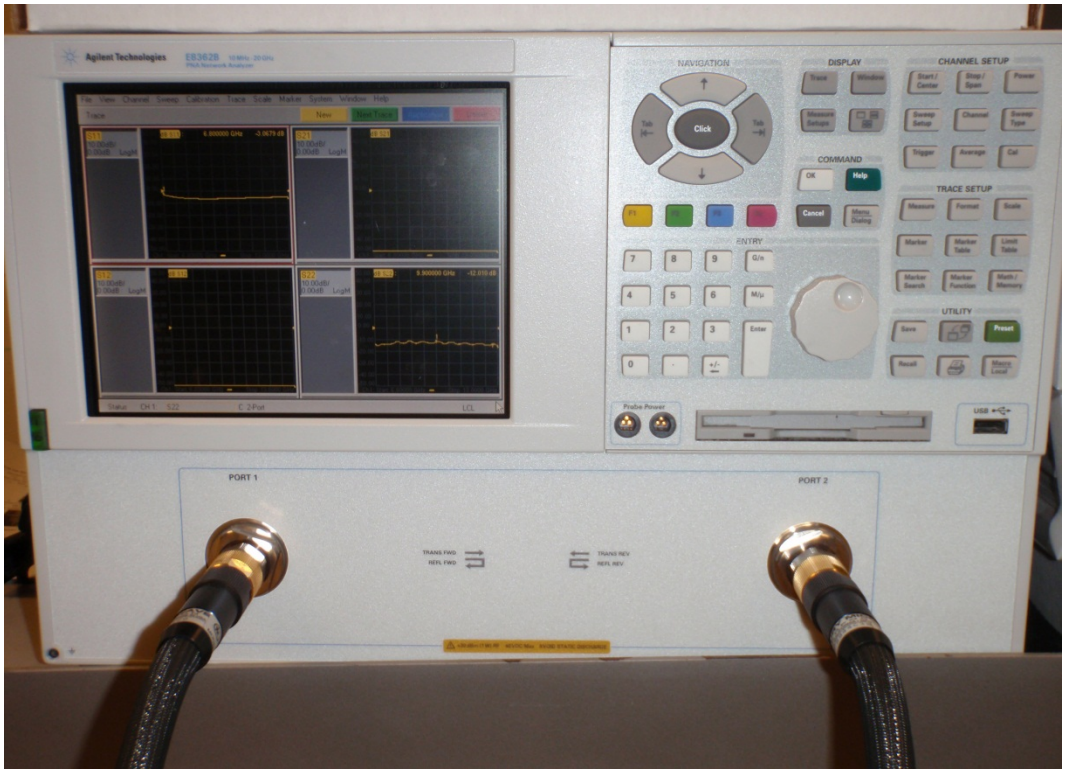

Figure 4.1: Network analyzer

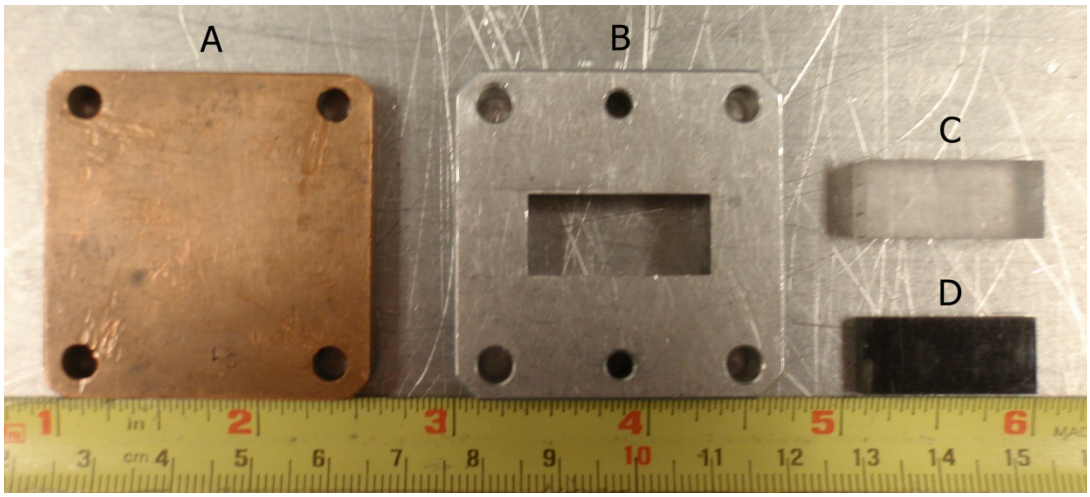

Figure 4.2: Short, sample holder, and materials

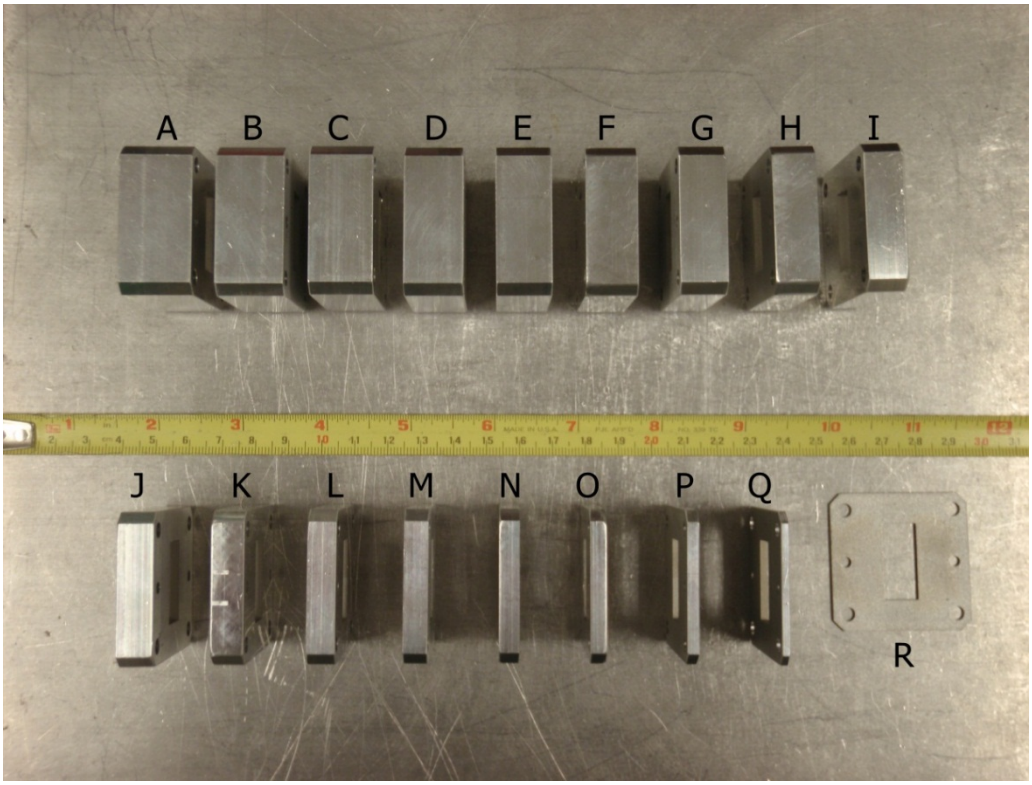

Figure 4.3: Shim offsets

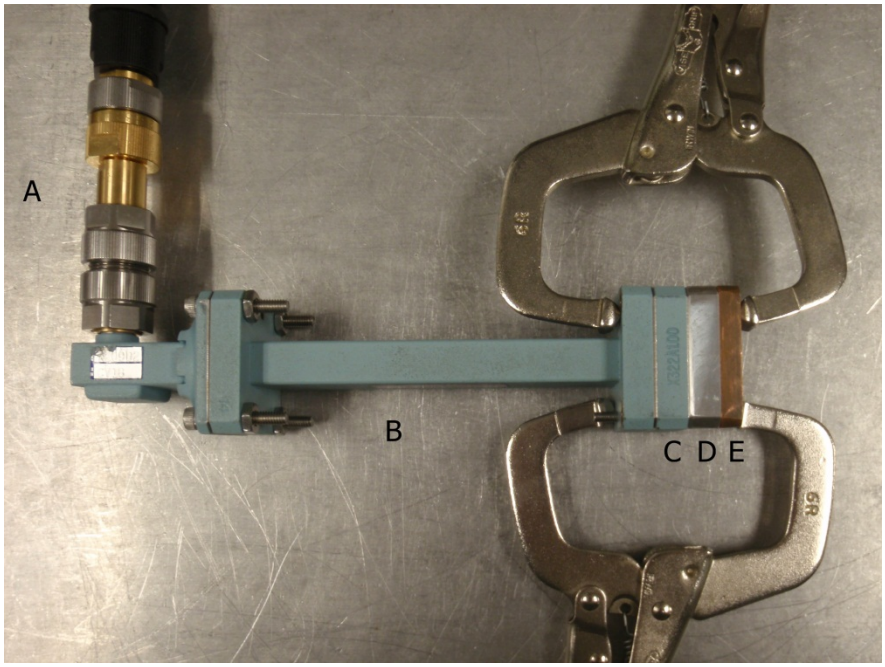

Figure 4.4: Single port measurements for the discrete approach

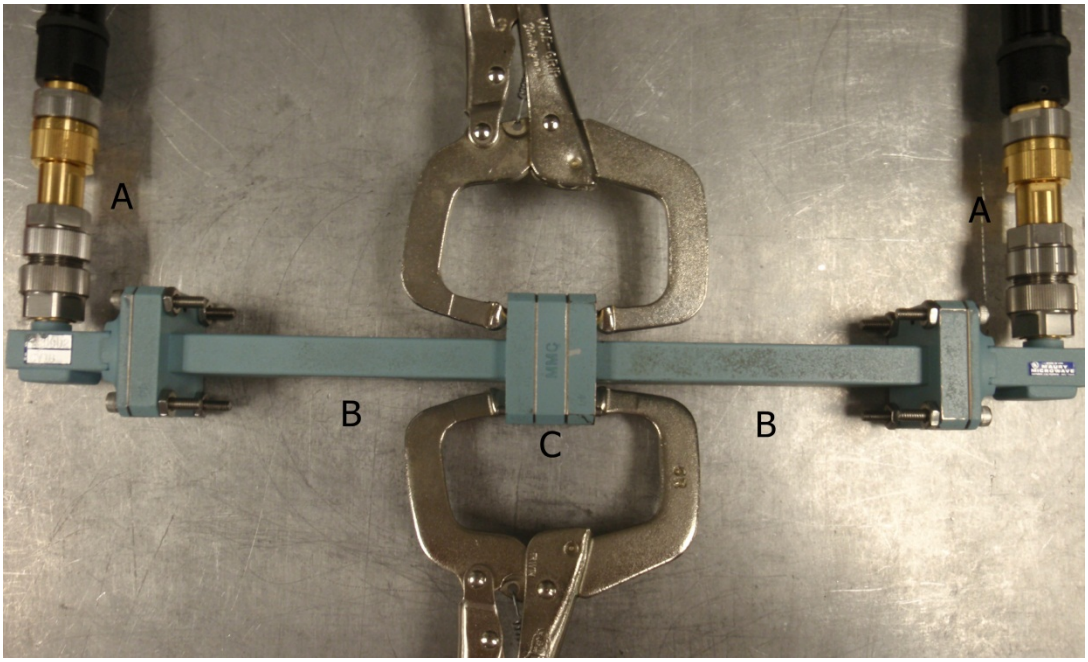

Figure 4.5: Two port measurement for the continuous approach

4.2 Calibration and Measurements

For both discrete and continuous measurement data sets, TRL calibration was used to ensure data accuracy. A brief description of TRL calibration theory is found in [6]. The network analyzer's built in TRL calibration kit was used prior to data collection.

A total of thirty eight measurements were taken for the discrete case when testing on a stratified material. This was done to find additional data points, and can only be accomplished for media that are sufficiently thinner than the sample holder to make these measurements possible. The stratified configuration is the only material that was tested in this way.

The first nineteen measurements were taken with the sample to the left of the sample holder. The next nineteen measurements were taken with the sample to the right of the sample holder. Figure 4.6 shows the two different measurement configurations.

The left side of the figure shows the sample to the left of the sample holder, and the right side of the figure shows the sample to the right of the sample holder. The figure also shows the waveguide (B), sample holder (C), shim (D), and short (E). In each set of measurements the short immediately followed the sample holder.

The first measurement was taken with no shim, and then measurements continued with the smallest shim (R in Figure 4.3). Each subsequent measurement was taken with an increasingly larger shim. The last measurement being the final shim (A in Figure 4.3). The first test of the discrete algorithm was using a stratified media with these thirty-eight measurements. This stratified media was comprised of a thin sample of Plexiglas, laminate material, and mica. At the end of taking all discrete measurements there were a total of thirty-eight data files, each containing the S_{11} scattering parameters associated with a given frequency. For the pseudo continuous inhomogeneous material, only nineteen measurements were possible since the material was too thick to create a right justified measurement set.

For the continuous case one two-port measurement was needed. In that instance the shims were not used. For these measurements an inhomogeneous material was constructed to collect the data as well as a homogeneous material for initial testing. In this instance, one file was created with S_{11}, S_{21}, S_{12}, and S_{22} scattering parameters associated with a given frequency.

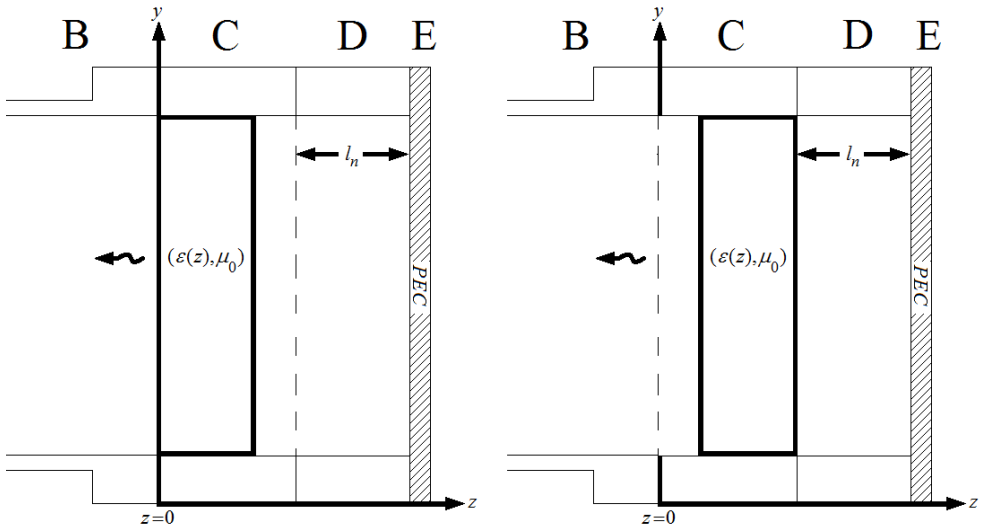

Figure 4.6: Left justified and right justified sample measurements

4.3 Error Analysis

The error analysis used in this section is similar the differential treatment in [5]. There are numerous sources of error when using these algorithms because they rely on experimental data for conducting the root search. This can be seen by revisiting the extraction formulae for the continuous case

$$\sum_i \left| \left[S_i^{thy}(\omega, \varepsilon_{r1}, m_\varepsilon) \right]^2 - \left[S_i^{\exp}(\omega) \right]^2 \right| < \delta \rightarrow \varepsilon_{r1}, m_\varepsilon, \tag{4.1}$$

and the discrete case

$$\sum_{l=1}^{L} \left| \left[S_{11,l}^{thy}(\omega, \varepsilon_1, ..., \varepsilon_N) \right]^2 - \left[S_{11,l}^{\exp}(\omega) \right]^2 \right| < \delta \rightarrow \varepsilon_n. \tag{4.2}$$

Not all errors are included in this discussion since many of them are difficult to measure and present minimal uncertainties. Examples of such errors include excessive movement of the coaxial cables, misalignment of the measuring constructs shown in

Figures (4.4) and (4.5), and uncertainties internal to the network analyzer. These are not investigated in this analysis.

Other errors can be approximated more easily and contribute more to the overall results and are used in the analysis. These include inaccuracies in material thickness measurements, placement of the material within the sample holder, and the uncertainty in the shim lengths for the discrete algorithm. The difference between the discrete and continuous case is that the continuous algorithm doesn't rely on shims and therefore has fewer sources of error in comparison.

Since the discrete case presents more error possibilities it is described in detail. The continuous case would follow a similar treatment without the shim measurement uncertainty.

The complex permittivity profile of the material can be written functionally as

$$\varepsilon = \varepsilon'(m, p, l) - j\varepsilon''(m, p, l). \tag{4.3}$$

This permittivity is comprised of a real component ε' and an imaginary component ε''. These are both functions of the material thickness *m*, the position of the material within the sample holder *p*, and the length of each shim *l*. There is uncertainty in each of these measurements leading to a perturbation from the actual permittivity profile

$$\Delta\varepsilon = \varepsilon'(m_0 + \Delta m, p_0 + \Delta p, l_0 + \Delta l) - j\varepsilon''(m_0 + \Delta m, p_0 + \Delta p, l_0 + \Delta l). \tag{4.4}$$

This equation shows that the uncertainty of the permittivity is a function of the actual measurements for the material, placement, and shim length denoted with the subscript *0,* and the uncertainty of these same measurements shown by Δm, Δp, and Δl.

The real permittivity could be written using a Taylor series as

$$\varepsilon'(m_0+\Delta m, p_0+\Delta p, l_0+\Delta l) = \varepsilon'(m_0, p_0, l_0) + \frac{\partial \varepsilon'(m_0, p_0, l_0)}{\partial m}\Delta m + \frac{\partial \varepsilon'(m_0, p_0, l_0)}{\partial p}\Delta p + \frac{\partial \varepsilon'(m_0, p_0, l_0)}{\partial l}\Delta l + ... \tag{4.5}$$

This is also true for the imaginary permittivity; however, to simplify the discussion only the real permittivity will be discussed. The imaginary permittivity uncertainty follows a similar process.

If the error is small, the higher order terms can be ignored in the Taylor series

$$\varepsilon'(m_0+\Delta m, p_0+\Delta p, l_0+\Delta l) - \varepsilon'(m_0, p_0, l_0) \approx \frac{\partial \varepsilon'(m_0, p_0, l_0)}{\partial m}\Delta m + \frac{\partial \varepsilon'(m_0, p_0, l_0)}{\partial p}\Delta p + \frac{\partial \varepsilon'(m_0, p_0, l_0)}{\partial l}\Delta l. \tag{4.6}$$

The partial derivatives can also be approximated if the errors are sufficiently small

$$\Delta\varepsilon'_m = \frac{\partial \varepsilon'(m_0, p_0, l_0)}{\partial m}\Delta m \approx \frac{\varepsilon'(m_0+\Delta m, p_0, l_0) - \varepsilon'(m_0, p_0, l_0)}{\Delta m}\Delta m, \tag{4.7}$$

$$\Delta\varepsilon'_p = \frac{\partial \varepsilon'(m_0, p_0, l_0)}{\partial p}\Delta p \approx \frac{\varepsilon'(m_0, p_0+\Delta p, l_0) - \varepsilon'(m_0, p_0, l_0)}{\Delta p}\Delta p, \tag{4.8}$$

$$\Delta\varepsilon'_l = \frac{\partial \varepsilon'(m_0, p_0, l_0)}{\partial l}\Delta l \approx \frac{\varepsilon'(m_0, p_0, l_0+\Delta l) - \varepsilon'(m_0, p_0, l_0)}{\Delta l}\Delta l. \tag{4.9}$$

The magnitude of each uncertainty is found and combined to find the total uncertainty in the resulting permittivity $\Delta\varepsilon'$ extracted by the algorithm

$$|\Delta\varepsilon'| = |\varepsilon'(m_0+\Delta m, p_0+\Delta p, l_0+\Delta l) - \varepsilon'(m_0, p_0, l_0)| \approx |\Delta\varepsilon'_m| + |\Delta\varepsilon'_p| + |\Delta\varepsilon'_l|. \tag{4.10}$$

The absolute values are used so that the errors associated with each uncertainty do not cancel with each other. This results in a total permittivity error that presents a worst case scenario regarding measurement errors.

The uncertainties Δm, Δp, and Δl can be positive or negative. For small uncertainties the resulting permittivity perturbations will be symmetric about $\varepsilon'(m_0, p_0, l_0)$. As the uncertainties increase the positive and negative errors can become significantly different from each other, and need to be calculated separately. It is assumed in this analysis that this difference is sufficiently small and does not warrant separate calculations. In this manner the uncertainties were calculated for the real and imaginary permittivity profiles for the discrete and continuous cases.

In the discrete case Δl was calculated by finding the standard deviation from the shim measurements, and using this uncertainty per shim during permittivity extraction. The material measurement errors (Δm), for the discrete and continuous cases were calculated using the standard deviation among material measurements, and depended on what material was being tested. The material placement error within the sample holder (Δp) was set to two tenths of mm for the calculations. These uncertainties will be seen on the graphs with the use of error bars.

4.4 Algorithm Results

This discussion starts with the results from the discrete case. These first graphs compare a material as measured within the stratified configuration (thin Plexiglas, laminate, and mica) with the inhomogeneous algorithm (red) and compare them with the same material that is measured individually using a homogeneous algorithm (blue) with a two-port scheme. Also note that each graph contains error bars for both the inhomogeneous and homogeneous algorithms using their respective color.

In Figure 4.7, Figure 4.8, and Figure 4.9 we see two graphs per figure. The first plots the real part of the relative permittivity versus frequency for both the inhomogeneous and homogeneous algorithms. The second plots the imaginary relative permittivity versus frequency for both the inhomogeneous and homogeneous algorithms. The figures are displayed in the order in which the materials are configured within the sample holder in the stratified configuration.

The first material encountered in the stratified media is Plexiglas. The real relative permittivity for Plexiglas is close to the actual value, but does differ at higher frequencies. The imaginary relative permittivity produced by the algorithm is strongly consistent with the actual imaginary relative permittivity. Immediately one can see the result error can play in the permittivity extraction using the discrete algorithm.

The second material in the stratified media was laminate. In the corresponding figure, a strong agreement with the imaginary results is seen, however again a slight divergence between the real permittivity in the inhomogeneous algorithm and the real permittivity in the homogeneous algorithm is seen.

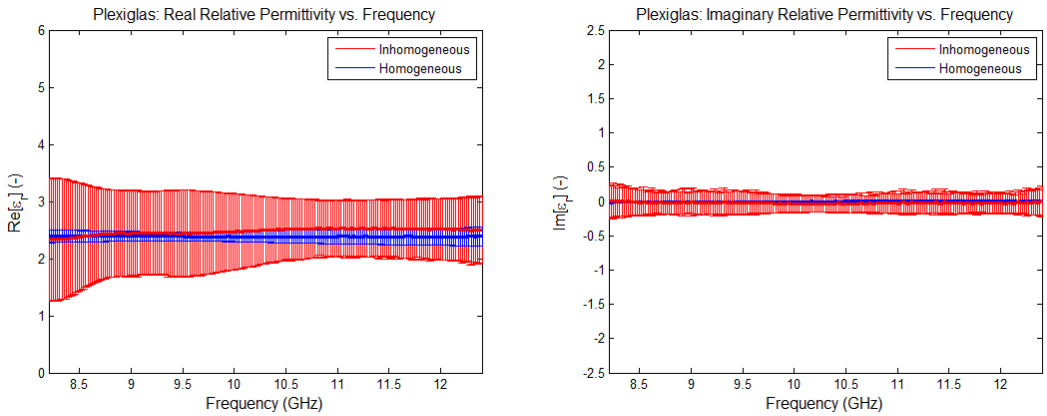

Figure 4.7: Real and imaginary results for Plexiglas

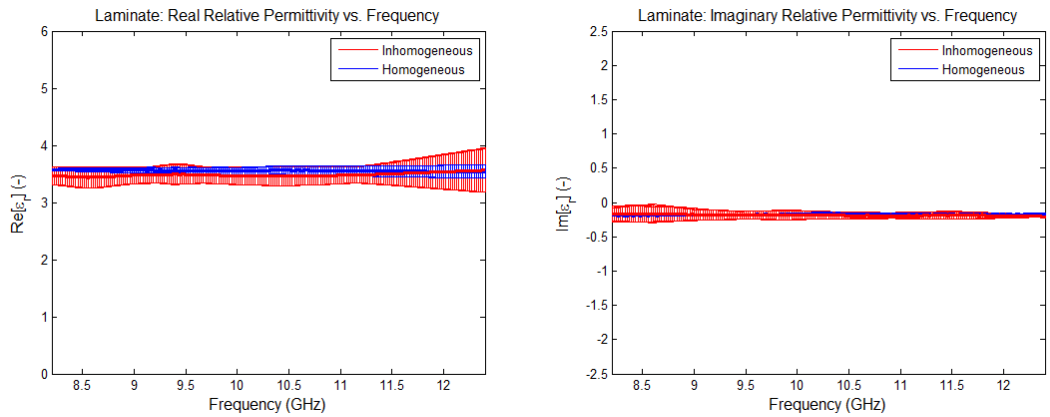

Figure 4.8: Real and imaginary results for laminate

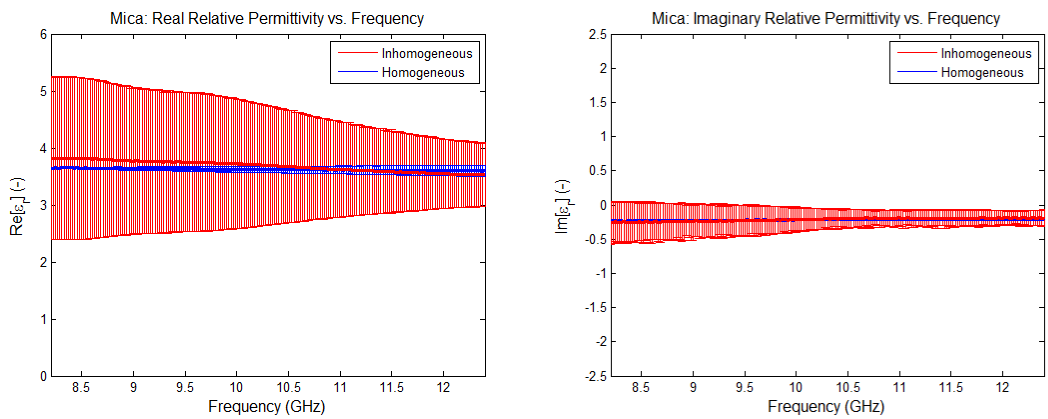

Figure 4.9: Real and imaginary results for mica

Finally, the third material encountered in the stratified sample is mica. There is again a slight divergence in the real permittivity results, and strong correlation in imaginary permittivity results.

Since there are over thirty-eight measurements in the discrete case, the cumulative effect of all uncertainties begins to increase the amount of error possible in the results. This can be easily seen when comparing the error bars between the inhomogeneous and homogeneous results. For this reason, great care must be taken when measuring the scattering parameters for the discrete case. This complex measurement environment is

believed to be the cause of the inaccuracies in the discrete algorithm. The smaller error seen in the imaginary calculations is believed to be caused by the fact that the material has relatively low loss. If the material has greater loss, it is likely the error bars would be just as large in the imaginary calculations as they are in the real calculations.

Next the results for the continuous case are discussed. This algorithm was tested with a homogeneous Plexiglas material and later with an inhomogeneous material created using layers of blue heavy-weight paper and yellow plastic.

The first test was a Plexiglas material to get a sense of accuracy with the algorithm. Since the material in region zero has a relative permittivity of one (free space) the z-intercept was assumed one, and only the slope was computed. For this comparison, the inhomogeneous slope was calculated with the continuous inhomogeneous algorithm and was plotted against the rise over run permittivity of the Plexiglas (calculated using homogeneous code). Figure 4.10 shows these results. Note that the slope is represented in these graphs as relative permittivity divided by distance in mm.

It can be seen from this figure that the real relative slope is fairly accurate, with a slight divergence above 11.5 GHz, and for the imaginary relative slope there is a smaller divergence. Since the mathematical solution of the differential equation in region two has an instability when slope is zero, a completely homogeneous material could not be used to test the algorithm to find both intercept and slope. Instead an inhomogeneous material was made for further testing.

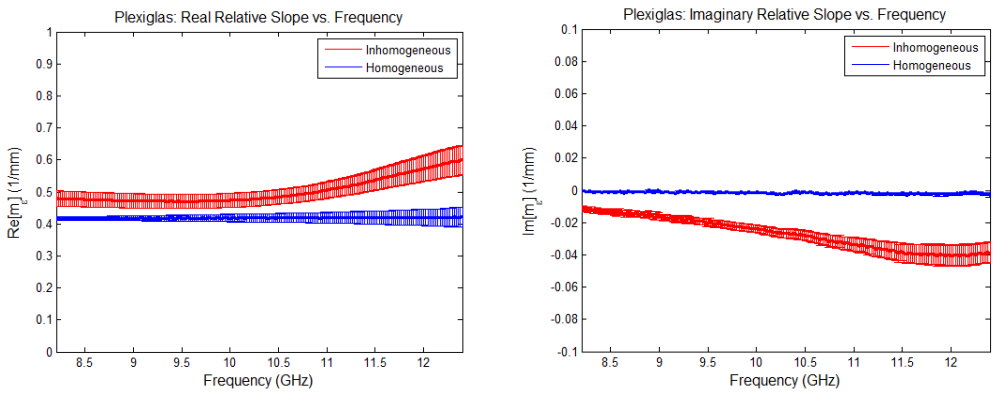

Figure 4.10: Real and imaginary relative slopes for Plexiglas

Next the continuous algorithm was tested with a pseudo continuous permittivity profile by interspersing layers of paper and plastic. For an adequate comparison paper and plastic were tested first as homogeneous materials. Figure 4.11 shows the real and imaginary permittivity results for paper, and Figure 4.12 shows the real and imaginary permittivity results for plastic. These figures show that paper has a larger permittivity and higher loss than plastic. By interspersing layers of paper and plastic an inhomogeneous material was constructed.

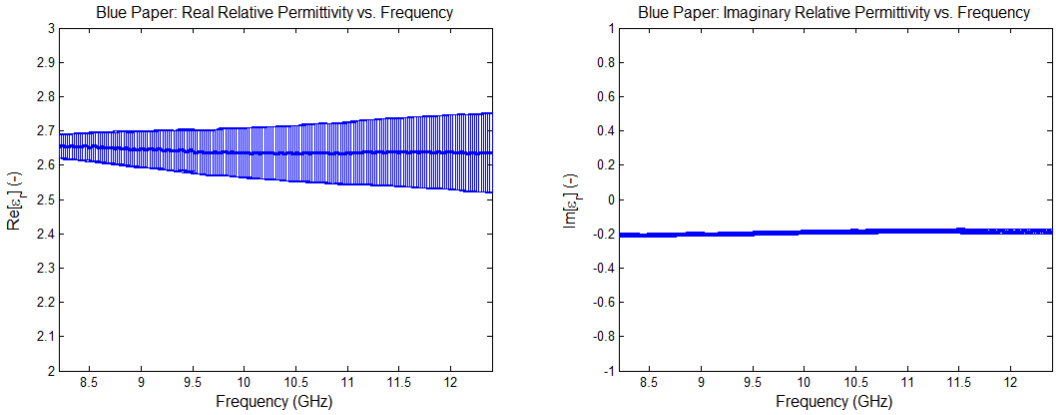

Figure 4.11: Real and imaginary results for blue paper

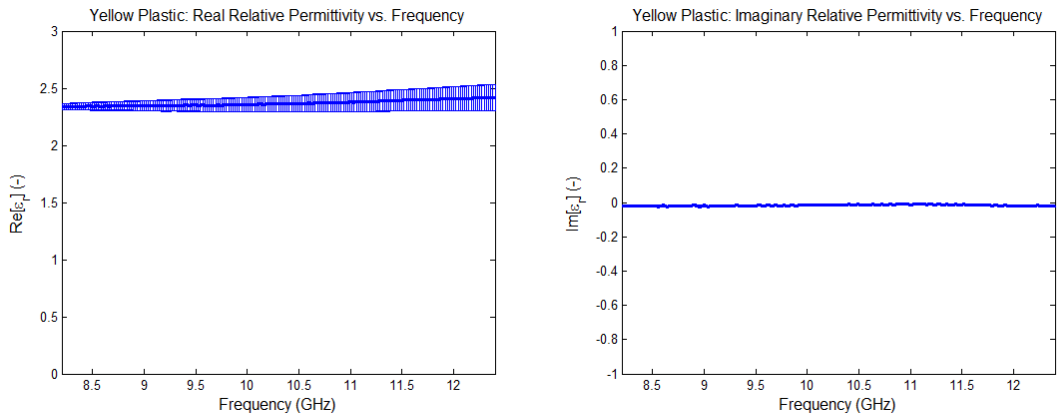

Figure 4.12: Real and imaginary results for yellow plastic

The inhomogeneous material was fashioned using five sub-layers, each with an increasingly larger number of paper layers until the last sub-layer contained only paper. Thus a material with an initial permittivity intercept and an increasing permittivity profile was created. Figure 4.13 shows the construction of the inhomogeneous material.

The material was fashioned so that it would fit securely inside the sample holder in the *x* and *y* directions. It was also clamped overnight to ensure that the layers were sandwiched tightly and the material's thickness in the *z* direction nearly uniform.

The material was tested so that the yellow plastic portion of the material began at the *z*=0 interface. And the material progressively increased in permittivity in the positive *z* direction (contains more and more blue paper layers). Figure 4.14 shows the results for the *z*-intercept. The extracted z-intercept from the inhomogeneous algorithm

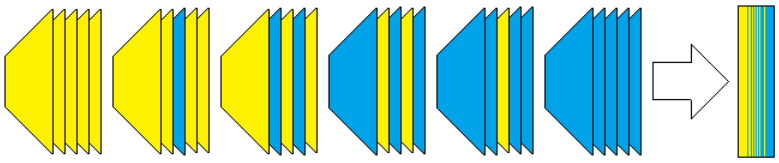

Figure 4.13: Plastic and paper inhomogeneous material construction

is shown in red and is compared to the permittivity of yellow plastic when calculated alone using the homogenous algorithm in blue. Both the real and imaginary parts of the relative intercept calculated by the inhomogeneous algorithm are fairly accurate. However, measurement error does not account for the discrepancy in the imaginary part of the permittivity intercept. One also sees that error plays a smaller role in the continuous algorithm when compared to the discrete algorithm.

Figure 4.15 shows the relative slope calculated by the inhomogeneous algorithm in red compared to the rise over run slope calculated from the homogeneous algorithms. Again, a strong consistency is seen between the inhomogeneous algorithm and the actual inhomogeneous permittivity of the material for both real and imaginary parts. It is also seen that the algorithm will converge with a material with a relatively small slope. The measurement errors again do not account for the slight divergence from the actual profile. These errors could be cause from inconsistencies during the fabrication process, since each thin slice of plastic or paper is not perfectly uniform.

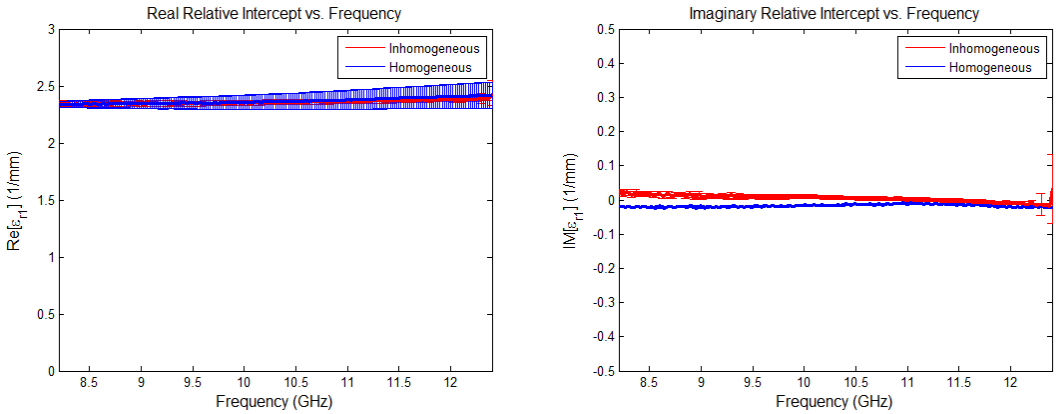

Figure 4.14: Continuous algorithm relative intercept results

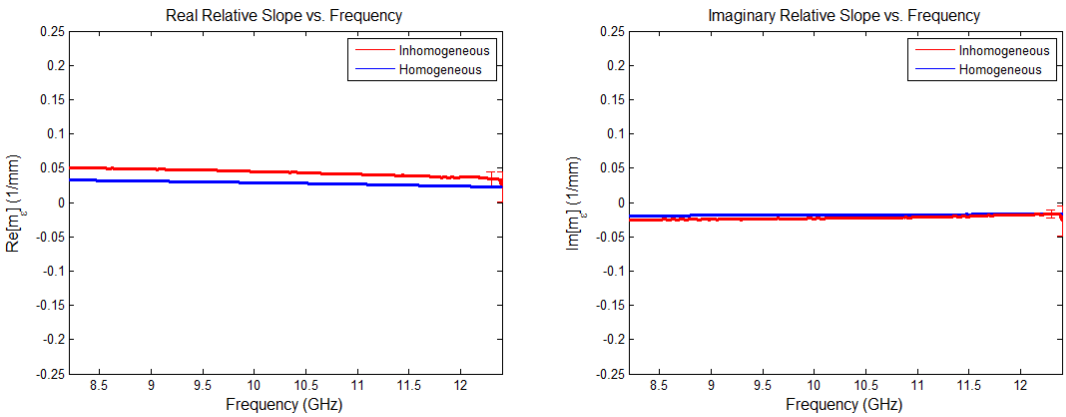

Figure 4.15: Continuous algorithm relative slope results

4.4 Discrete and Continuous Algorithm Comparison

Figures (4.16) and (4.17) show the continuous and discrete algorithm profiles compared to the actual profile described in Figure 4.13. In both graphs, the inhomogeneous algorithm profile is shown in red, and the actual profile in blue. The left graph in Figure 4.16 shows the real part of $e_r(z)$ versus z in mm, and the right graph shows the imaginary part of $e_r(z)$ versus z in mm. All plots are done using the mid-band frequency of 10 GHz. The results of the continuous algorithm on the real graph show strong agreement at $z=0$, but the algorithm starts to diverge from the actual profile as $z \rightarrow d_0$. The results in the imaginary graph are most accurate in the center of the material, but the algorithm diverges from the actual profile as $z \rightarrow 0$ or $z \rightarrow d_0$.

Figure 4.17 shows the accuracy of the discrete algorithm. For this material only left justified measurements were taken since the material was too thick to also do right justified measurements. The discrete algorithm closely follows the actual profile, except that at the edges of each step it becomes less accurate. The large uncertainty possibilities are also seen in this figure, especially for the ε_2 section.

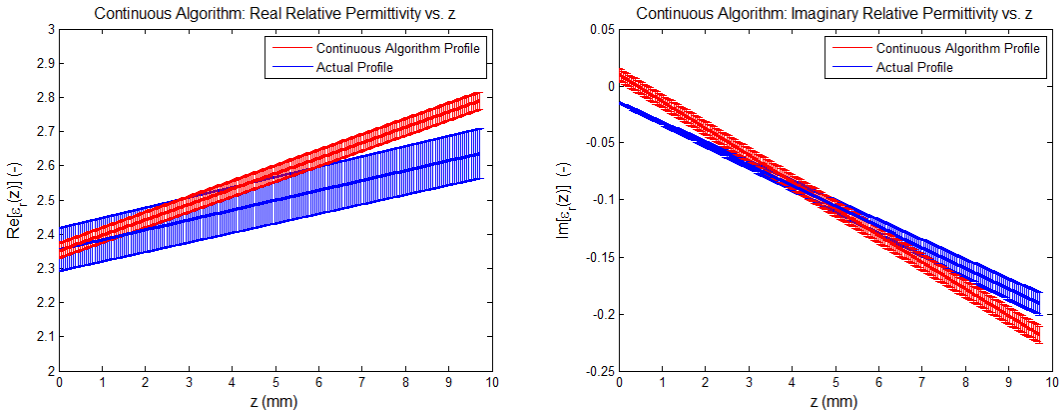

Figure 4.16: Continuous algorithm profile results

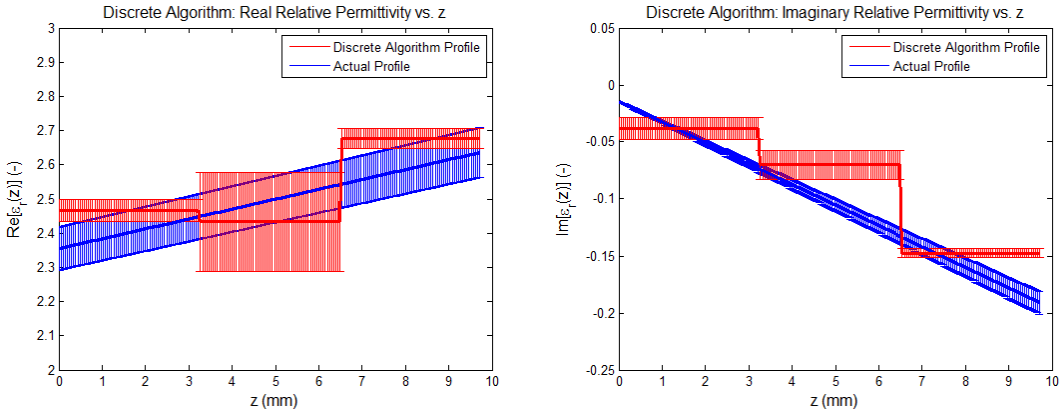

Figure 4.17: Discrete algorithm profile results

If one were to use a homogeneous algorithm to find the profile of this same inhomogeneous material the results would be similar to what is shown in Figure 4.18 and Figure 4.19. These show the permittivity as a function of frequency. In Figure 4.20 and Figure 4.21 the permittivity is plotted versus position z within the material at the mid-band frequency of 10 GHz.

Despite some of the inaccuracies associated with the discrete and continuous profiles, they still better articulate the changing profile within the material.

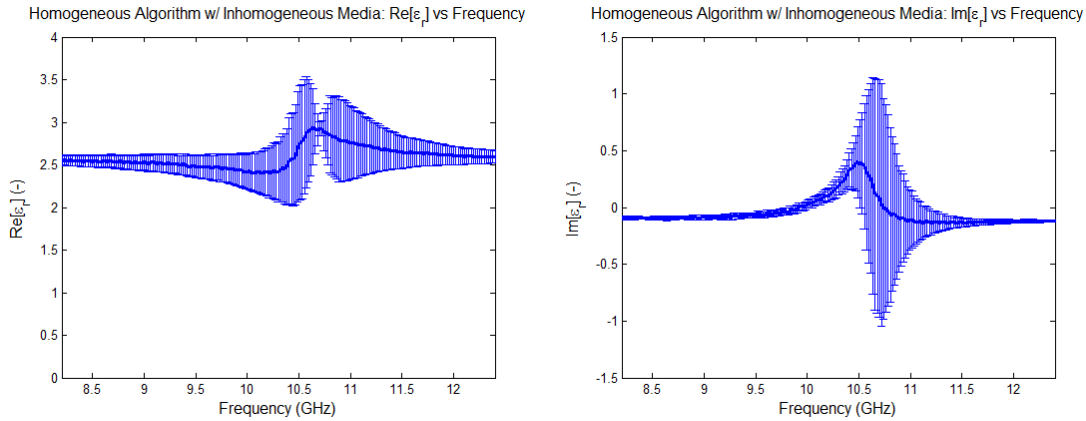

Figure 4.18: Inhomogeneous material characterized with homogeneous algorithm

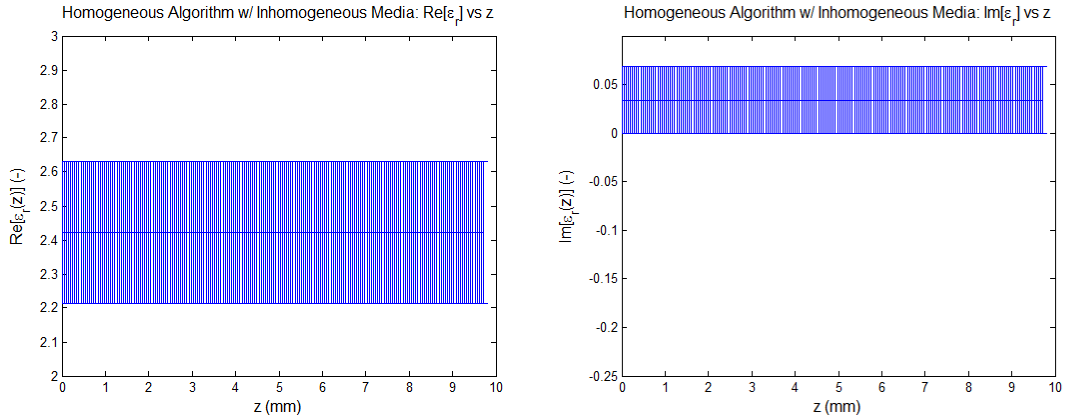

Figure 4.18: Inhomogeneous material profiled with homogeneous algorithm

The discrete and continuous algorithms have their own benefits and drawbacks. The discrete algorithm's advantages include its ability to characterize a material with a simpler theoretical foundation since it relies on homogeneous wave equations. It also becomes advantageous if one were to characterize a material that is not linear, since it would likely provide a more accurate result in comparison to the continuous profile because it splits up the material into sections. This approach also lends itself easily to characterizing layered stack material configurations such as a Jaumann absorber.

A major disadvantage of the discrete algorithm is the resulting profile averages across sections within the material. This produces inaccuracies at each permittivity section's right and left boundaries. Also, the discrete algorithm is more error prone as can be seen by the error bars.

One could potentially change the discrete code so that it produces a finer characterization with additional sections, but it was discovered during testing that as the section numbers were increased the accuracy of the algorithm began to sharply diminish. This could be caused by an inability of the network analyzer to distinguish between the phase differences from each shim. A more precise measuring device or additional data points would allow for a greater set of independent equations for the Levenberg-Marquardt root search. It is also possible that an alternative root search method other than Levenberg-Marquardt could provide better results. The convergence of the algorithm becomes increasingly temperamental with additional root search dimensions.

The continuous approach is advantageous over the discrete approach in some ways including the fact that it produces a smoother profile characterization. It also requires only one measurement, so that it takes less effort and time to collect the algorithm's necessary data points. Also, with one measurement there is a lower likelihood of error creeping into the resulting profile.

A disadvantage of this approach in comparison to the discrete method is that it requires a more complex theoretical foundation as seen in Chapter 3. Additionally, this approach would do a poorer job than the discrete approach when characterizing a non-linear inhomogeneous profile. Another disadvantage of the continuous algorithm is that

the theoretical development produced equations with an instability as $m_\varepsilon \to 0$ as seen from (3.19) or (3.20). When characterizing materials with very low slopes a check is necessary within the algorithm to ensure that the equations do not become too large and lead to an erroneous profile characterization.

The continuous approach will not scale well with thick materials since it was assumed from the beginning of the development that the material was thin. To characterize thicker material's more complex theoretical profiles need to be assumed instead of the linear profile used in (3.15).

4.5 Summary

This chapter discussed the equipment used for data collection and the results from the discrete and continuous algorithms using several testing scenarios. Both the discrete and continuous algorithms produced adequate profile characterizations of the test materials. However, in some regions within the material they produced slight inaccuracies in comparison to the actual permittivity profile.

The discrete and continuous algorithms have advantages and disadvantages depending on how they are implemented and what materials are being characterized. Some basic understanding of the material being investigated is beneficial in selecting the best method to use. In the next chapter the entire study will be summarized.

V. Conclusion

This document discussed the theoretical formulation for developing a discrete and continuous algorithm to find inhomogeneous permittivity profiles. It revealed the algorithms' results when testing on various materials and the pros and cons of each.

The discrete approach offered a theoretically simpler framework since it relied on homogeneous wave equations in a piece-wise constant permittivity approach. However, there was a significant downside to this approach since it required numerous measurements to implement. This can lead to gross error in the results if measurements are not taken accurately.

The continuous approach offered a way of creating a smooth permittivity profile using inhomogeneous wave equations. This required only one measurement, but relies on a more complex development and a thin material assumption. Unfortunately, this continuous algorithm may give misleading results for thicker materials.

Despite some of the drawbacks associated with either technique, they still offer a reasonable solution to inhomogeneous permittivity characterization. Depending on the material, one may choose one method or the other.

5.1 Future Research

Improvements can be made to each approach presented in this study. For the discrete case one could improve the precision of the permittivity profile solutions. This could be done by using additional measurement data, a one port calibration technique to reduce noise, or an alternative root search method. During the shim calculations a ten

degrees phase was used for each shim thickness. If it is possible to use a smaller phase spacing with a device capable of distinguishing these phase differences, more independent measurements can be included in the algorithm for a more detailed profile result.

The continuous case can also be improved. In this study the material was assumed to be thin, and the profile approximated as a linear function. Work could be done to investigate permittivity profiles of thicker materials, or ones that have parabolic, sinusoidal, or more complicated permittivity profiles.

Additionally, both approaches found only inhomogeneous permittivity profiles. These developments could be expanded to include permeability inhomogeneity as well. These approaches could also be combined in the future to produce an algorithm that would solve for a piece-wise linear profile. This would allow the characterization of more complicated profiles.

Appendix A: Constitutive parameter extraction main code example

```
%Written by: Capt Marcus A Sitterly
%Date: 19 July 11
%Sample Code for constitutive parameter extraction for one material

%CONSTANTS USED IN CALCULATIONS
epsilonnot = (10^-9)/(36*pi);       %F/m
munot = 4*pi*10^-7;                 %H/m
a = 2.286*10^-2;                    %'a' dimension in m for WR90
length1 = 6.64*10^-3;               %length of sample of thick
Plexiglas

%DATA MANIPULATION BEFORE INPUT TO LEVENBERG-MARQUAD ALGORITHM

%Read in laboratory data from text file with custom function
[ frequency S11exp S21exp S12exp S22exp ] =
dataextract('plexi_thick.txt');

omega = 2*pi*frequency;             %Angular Frequency
k0 = omega*sqrt(epsilonnot*munot);  %Propogation constant k
kz0 = sqrt((k0.^2)-(pi/a)^2);       %Propogation constant kz


%Measurements derived from lab with phase shift
S11exp = S11exp;
S12exp = S12exp.*exp(-j.*kz0.*length1);
S21exp = S21exp.*exp(-j.*kz0.*length1);
S22exp = S22exp.*exp(-2.*j.*kz0.*length1);

%Allocate space for epsilonrel1 and murel1 vectors
epsilonrel1 = zeros(length(frequency),1);
murel1 = zeros(length(frequency),1);

%CALCULATE EPSILON RELATIVE AND MU RELATIVE FOR GIVEN FREQUENCY
for t=1:length(frequency)

%Experimental values derived from lab [S11 S12 S21 S22] for Plexiglas
y =[S11exp(t) S12exp(t) S21exp(t) S22exp(t)];

%Vector that contains frequency and length measurement for algorithm
x=[omega(t) length1];

%Initial guess [epsilonrel1 murel1]
betanot= [3,1];

%Use NLFIT to obtain epsilon/mu
beta=nlinfit(x,y,@onematerial,betanot);
```

```
%Assign epsilon and mu values from numerical calculation
epsilonrel1(t)=beta(1);
murel1(t)=beta(2);

end

%PLOT RESULTS

%Plot real(e) vs frequency
figure(1);
plot((10^-9)*frequency,(real(epsilonrel1)));
axis([min((10^-9)*frequency) max((10^-9)*frequency) 0 3]); % axis([xmin
xmax ymin ymax])
title('FREQUENCY VS. REAL \epsilon_r', 'fontsize', 12)
xlabel('Frequency (GHz)', 'fontsize', 12);
ylabel('Re(\epsilon_r)', 'fontsize', 12);

%Plot imag(e) vs frequency
figure(2);
plot((10^-9)*frequency,(imag(epsilonrel1)));
axis([min((10^-9)*frequency) max((10^-9)*frequency) -1 1]); %
axis([xmin xmax ymin ymax])
title('FREQUENCY VS. IMAGINARY \epsilon_r', 'fontsize', 12)
xlabel('Frequency (GHz)', 'fontsize', 12);
ylabel('Im(\epsilon_r)', 'fontsize', 12);

%Plot real(mu) vs frequency
figure(3);
plot((10^-9)*frequency,(real(murel1)));
axis([min((10^-9)*frequency) max((10^-9)*frequency) 0 2]); % axis([xmin
xmax ymin ymax])
title('FREQUENCY VS. REAL \mu_r', 'fontsize', 12)
xlabel('Frequency (GHz)', 'fontsize', 12);
ylabel('Re(\mu_r)', 'fontsize', 12);

%Plot imag(mu) vs frequency
figure(4);
plot((10^-9)*frequency,(imag(murel1)));
axis([min((10^-9)*frequency) max((10^-9)*frequency) -1 1]); %
axis([xmin xmax ymin ymax])
title('FREQUENCY VS. IMAGINARY \mu_r', 'fontsize', 12)
xlabel('Frequency (GHz)', 'fontsize', 12);
ylabel('Im(\mu_r)', 'fontsize', 12);
```

Appendix B: Code for nlinfit function

```
function y=onematerial(betanot,x)

a = 2.286*10^-2;                %'a' dimension in m for  WR-90
omega = x(1);                   %Angular Frequency
epsilonnot = (10^-9)/(36*pi);   %F/m
munot = 4*pi*10^-7;             %H/m

% MATERIAL SLICES PARAMETERS

%Material
epsilonrel1 = betanot(1);       %betanot(1) is algorithms value for
epsilon
murel1 = betanot(2);            %betanot(2) is algorithms value for mu
length1 = x(2);

%Last interface (free space)
epsilonrel2 = 1;
murel2 = 1;
lengthend = 0;


%PROPOGATION CONSTANT CALCULATIONS
%Propagation constant k
k0 = omega*sqrt(epsilonnot*munot);
k1 = omega*sqrt(epsilonrel1*epsilonnot*murel1*munot);
k2 = omega*sqrt(epsilonrel2*epsilonnot*murel2*munot);

%Propagation constant kz
kz0 = sqrt((k0^2)-(pi/a)^2);
kz1 = sqrt((k1^2)-(pi/a)^2);
kz2 = sqrt((k2^2)-(pi/a)^2);

%IMPEDANCE CALCULATIONS
%Material impedance calculations
eta0 = sqrt(munot/epsilonnot);
eta1 = sqrt((murel1*munot)/(epsilonrel1*epsilonnot));
eta2 = sqrt((murel2*munot)/(epsilonrel2*epsilonnot));

%Wave impedance calculations
waveimpedence0 = (eta0*k0)/kz0;
waveimpedence1 = (eta1*k1)/kz1;
waveimpedence2 = (eta2*k2)/kz2;

R1 = (waveimpedence1 - waveimpedence0)/(waveimpedence1 +
waveimpedence0);
R2 = (waveimpedence2 - waveimpedence1)/(waveimpedence2 +
waveimpedence1);
```

```
P1 = exp(-j*kz1*length1);
P2 = exp(-j*kz2*lengthend);

%A MATRIX CALCULATIONS
A1 = (1/(P1*(1+R1)))*[1 (R1*P1^2);R1 P1^2];
A2 = (1/(P2*(1+R2)))*[1 (R2*P2^2);R2 P2^2];

%Find A Matrix for the system
ASys = A1*A2;
A11 = ASys(1,1);
A12 = ASys(1,2);
A21 = ASys(2,1);
A22 = ASys(2,2);

%Find the S matrix from the A matrix
SSys = (1/A11)*[A21 (A11*A22-A21*A12);1 -A12];
S11 = SSys(1,1);
S12 = SSys(1,2);
S21 = SSys(2,1);
S22 = SSys(2,2);

%Compare to labratory data
y = [S11 S12 S21 S22];
```

Bibliography

1. Attaway, Stormy. *Matlab: A Practical Introduction to Programming and Problem Solving*. Burlington, Massachusetts: Elsevier Academic Press, 2009.

2. Balanis, Constantine A. *Advanced Engineering Electromagnetics*. New York: John Wiley & Sons, 1989.

3. Burden, Richard L. and J. Douglas Faires. *Numerical Analysis* (9th Edition). Boston: Brooks/Cole, 2011.

4. Chew, Weng C. *Waves and Fields in Inhomogeneous Media*. New York: IEEE Press, 1995.

5. Dorey, Sean. "Stepped Waveguide Electromagnetic Material Characterization Technique," M.S. Thesis, Air Force Institute of Technology, Dayton, Ohio, 2004.

6. Glenn F. Engen and Cletus A. Hoer. "'Thru-Reflect-Line': An Improved Technique for Calibrating the Dual Six-Port Automatic Network Analyzer," *IEEE Trans. Microwave Theory and Techniques,* vol. MTT-27, No. 12, pp. 987-993, Dec. 1979.

7. Havrilla, Michael J. "Analytical and experimental techniques for the electromagnetic characterization of materials," PH.D. dissertation, Michigan State University, East Lansing, Michigan, 2001.

8. Havrilla, Michael J. and Dennis P. Nyquist. "Electromagnetic Characterization of Layered Materials via Direct and De-embed Methods." *IEEE Trans. Instrumentation and Measurement,* vol. 55, no. 1, pp. 158-162, Feb. 2006.

9. Nicolson, A. M. and G. F. Ross. "Measurement of the Intrinsic Properties of Materials by Time-Domain Techniques," *IEEE Trans. Instrumentation and Measurement*, vol. IM-19, No. 4, pp. 337-382, Nov. 1970.

10. Polyanin, Andrei D. and Alexander V. Manzhirov. *Handbook of Mathmematics for Engineers and Scientists*. Boca Raton, Florida: Chapman & Hall/CRC, 2007.

11. Tyras, George. *Radiation and Propagation of Electromagnetic Waves*. London: Academic Press, Inc., 1969.

12. Wier, William B. "Automatic measurement of complex dielectric constant and permeability at microwave frequencies," *Proc. IEEE*, vol. 62, pp. 33-36, Jan. 1974.

REPORT DOCUMENTATION PAGE

Form Approved
OMB No. 074-0188

The public reporting burden for this collection of information is estimated to average 1 hour per response, including the time for reviewing instructions, searching existing data sources, gathering and maintaining the data needed, and completing and reviewing the collection of information. Send comments regarding this burden estimate or any other aspect of the collection of information, including suggestions for reducing this burden to Department of Defense, Washington Headquarters Services, Directorate for Information Operations and Reports (0704-0188), 1215 Jefferson Davis Highway, Suite 1204, Arlington, VA 22202-4302. Respondents should be aware that notwithstanding any other provision of law, no person shall be subject to an penalty for failing to comply with a collection of information if it does not display a currently valid OMB control number.
PLEASE DO NOT RETURN YOUR FORM TO THE ABOVE ADDRESS.

1. REPORT DATE *(DD-MM-YYYY)*	2. REPORT TYPE	3. DATES COVERED *(From – To)*
22-03-2012	Master's Thesis	Sep 2010 – March 2012

4. TITLE AND SUBTITLE
ELECTROMAGNETIC CHARACTERIZATION OF INHOMOGENEOUS MEDIA

5a. CONTRACT NUMBER

5b. GRANT NUMBER

5c. PROGRAM ELEMENT NUMBER

6. AUTHOR(S)
Sitterly, Marcus A., Captain, USAF

5d. PROJECT NUMBER

5e. TASK NUMBER

5f. WORK UNIT NUMBER

7. PERFORMING ORGANIZATION NAMES(S) AND ADDRESS(S)
Air Force Institute of Technology
Graduate School of Engineering and Management (AFIT/EN)
2950 Hobson Way, Building 640
WPAFB OH 45433-8865

8. PERFORMING ORGANIZATION REPORT NUMBER
AFIT/GE/ENG/12-37

9. SPONSORING/MONITORING AGENCY NAME(S) AND ADDRESS(ES)
Air Force Research Laboratory, Sensors Directorate
2591 K Street, Bldg. 254
Wright-Patterson AFB, OH 45433-7602

10. SPONSOR/MONITOR'S ACRONYM(S)
Fill in

11. SPONSOR/MONITOR'S REPORT NUMBER(S)

12. DISTRIBUTION/AVAILABILITY STATEMENT
APPROVED FOR PUBLIC RELEASE; DISTRIBUTION UNLIMITED.

13. SUPPLEMENTARY NOTES
This material is declared a work of the U.S. Government and is not subject to copyright protection in the United States

14. ABSTRACT
Developed two permittivity profile extraction algorithms for inhomogeneous materials. These two algorithms were created using discrete and continuous approaches.

The discrete method used a piece-wise constant permittivity assumption that allowed the use of homogeneous wave equations. Using laboratory data and a theoretical formulation, the permittivity of each piece-wise constant layer within the material was extracted using a root search algorithm.

The continuous approach solved the problem using inhomogeneous wave equations. These equations were used to extract a linear permittivity profile using laboratory data and a root search.

15. SUBJECT TERMS
Inhomogeneous, Permittivity, Waveguide, X-band

16. SECURITY CLASSIFICATION OF: Unclassified			17. LIMITATION OF ABSTRACT	18. NUMBER OF PAGES	19a. NAME OF RESPONSIBLE PERSON
a. REPORT	b. ABSTRACT	c. THIS PAGE			Dr. Michael J. Havrilla (ENG)
U	U	U	UU	78	19b. TELEPHONE NUMBER *(Include area code)* (937) 255-3636, ext 7252 michael.havrilla@afit.edu

Standard Form 298 (Rev. 8-98)
Prescribed by ANSI Std. Z39-18